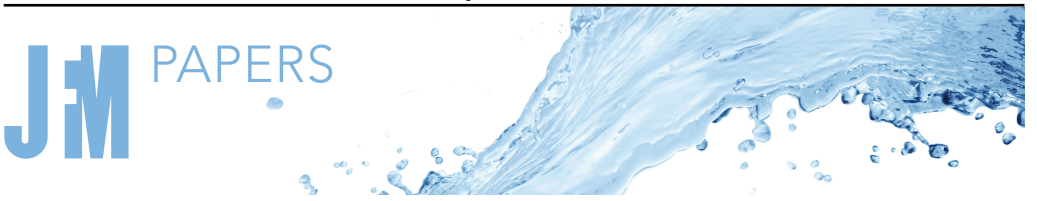
J. Fluid Mech. (2026), *vol.* 1032, A16, doi:10.1017/jfm.2026.11358



Controlled particle displacement by hydrodynamic obstacle interaction in non-inertial flows

Partha Kumar Das[1], **Xuchen Liu**[1] **and Sascha Hilgenfeldt**[1]

[1]Department of Mechanical Science and Engineering, The Grainger College of Engineering, University of Illinois Urbana-Champaign, Urbana, IL 61801, USA

Corresponding author: Sascha Hilgenfeldt, sascha@illinois.edu

(Received 10 November 2025; revised 16 January 2026; accepted 22 February 2026)

Systematic deflection of microparticles off of initial streamlines is a fundamental task in microfluidics, aiming at applications including sorting, accumulation or capture of the transported particles. In a large class of set-ups, including deterministic lateral displacement and porous media filtering, particles in non-inertial (Stokes) flows are deflected by an array of obstacles. We show that net deflection of force-free particles passing an obstacle in Stokes flow is possible solely by hydrodynamic interactions if the flow and obstacle geometry break fore–aft symmetries. The net deflection is maximal for certain initial conditions and we analytically describe its scaling with particle size, obstacle shape and flow geometry, confirmed by direct trajectory simulations. For realistic parameters, separation by particle size is comparable to what is found assuming contact (roughness) interactions. Our approach also makes systematic predictions on when short-range attractive forces lead to particle capture or sticking. In separating hydrodynamic effects on particle motion strictly from contact interactions, we provide novel, rigorous guidelines for elementary microfluidic particle manipulation and filtering.

Key words: low-Reynolds-number flows, general fluid mechanics, microfluidics

1. Introduction

Microfluidic technologies have revolutionised particle manipulation, offering a diverse array of capabilities including transportation, separation, trapping and enrichment (Pratt *et al.* 2011; Sajeesh & Sen 2014; Lu *et al.* 2017). Fundamentally, manipulation strategies force particles to cross streamlines so that they do not passively follow the flow. This essence of controlled manipulation, encompassing both passive (synthetic) or active (e.g.

© The Author(s), 2026. Published by Cambridge University Press. This is an Open Access article, distributed under the terms of the Creative Commons Attribution licence (https://creativecommons.org/licenses/by/4.0/), which permits unrestricted re-use, distribution and reproduction, provided the original article is properly cited.

https://doi.org/10.1017/jfm.2026.11358 Published online by Cambridge University Press

biological cells) particles, is implemented today in lab-on-a-chip processing as well as in the diagnosis of biological samples and biomanufacturing processes (Pamme 2007; Ateya *et al.* 2008; Nilsson *et al.* 2009; Gossett *et al.* 2010; Xuan, Zhu & Church 2010; Puri & Ganguly 2014), drug discovery and delivery systems (Dittrich & Manz 2006; Kang *et al.* 2008; Nguyen *et al.* 2013) or self-cleaning technologies (Callow & Callow 2011; Kirschner & Brennan 2012; Nir & Reches 2016). Many techniques of precise control of suspended microparticles rely on the particle response to external forces including electrical (Xuan 2019), optical (Lenshof & Laurell 2010; Ashkin *et al.* 1986; Grier 2003; Chiou, Ohta & Wu 2005) and magnetic (Van Reenen *et al.* 2014; Crick & Hughes 1950; Wang, Butler & Ingber 1993; Gosse & Croquette 2002) techniques. However, not all particles are susceptible to these, prompting a continuous interest in manipulation strategies solely based on hydrodynamic forces. In practical applications, these approaches use customised flow geometries, such as channels or pillars (Lutz, Chen & Schwartz 2006; Tanyeri *et al.* 2011; Wiklund, Green & Ohlin 2012; Petit *et al.* 2012; Shenoy, Rao & Schroeder 2016; Kumar *et al.* 2019; Chamolly, Lauga & Tottori 2020). In recent years, many such techniques have leveraged particle inertia (Di Carlo *et al.* 2007; Di Carlo 2009) particularly from oscillatory flow (Wang *et al.* 2011, 2012; Thameem, Rallabandi & Hilgenfeldt 2017; Agarwal, Rallabandi & Hilgenfeldt 2018) and have prompted an advance of theoretical frameworks beyond long-standing approaches (Maxey & Riley 1983; Gatignol 1983) to include new important effects (Agarwal *et al.* 2021; Agarwal 2021; Rallabandi 2021; Agarwal *et al.* 2024).

Inertial effects are not present in the Stokes limit (Reynolds number $Re \to 0$), where hydrodynamic effects on particles are notoriously long-range and have been described in fundamental detail (Happel & Brenner 1965; Brady & Bossis 1988; Kim & Karrila 2013; Pozrikidis 1992, 2011; Rallabandi, Hilgenfeldt & Stone 2017), while systematic modulation of particle trajectories in Stokes flow has not been the subject of a detailed study. Fundamentally, this is because of the instantaneity and time reversibility of Stokes flow that at first glance seems to preclude lasting particle displacements, despite the success of deterministic lateral displacement (DLD) in sorting particles by size, forcing them onto different trajectories through the interaction with a forest of pillar obstacles at very low Re (Huang *et al.* 2004; Krüger *et al.* 2014; Kabacaoğlu & Biros 2019; Hochstetter *et al.* 2020; Lu *et al.* 2023; Aghilinejad *et al.* 2019; Davis *et al.* 2006).

Size-based particle sorting in a typical DLD set-up is determined by whether a particle can cross separating streamlines (row-shift). Inglis *et al.* (2006), Kulrattanarak *et al.* (2011), Pariset *et al.* (2017), Cerbelli (2012) and Aghilinejad *et al.* (2019) heuristically developed critical length scales for particle size above which lateral displacement by this row-shifting happens. Modelling approaches for the interaction of particles with individual obstacles generally appeal to contact forces or other strong short-range forces (Lin & Han 2002; Dance, Climent & Maxey 2004) that break the time reversibility of the Stokes flow and the hydrodynamic forces following from it. In particular, Frechette & Drazer (2009), Balvin *et al.* (2009) and Bowman, Drazer & Frechette (2013) modelled the effects of a non-hydrodynamic repulsive force originating from surface roughness (Ekiel-Jeżewska *et al.* 1999) and its dependence on particle size. This approach has been informed by similar ideas in the modelling of suspension rheology (Da Cunha & Hinch 1996; Metzger & Butler 2010; Blanc, Peters & Lemaire 2011; Pham, Metzger & Butler 2015; Lemaire *et al.* 2023).

Contact forces almost invariably contain an *ad hoc* element (Ekiel-Jeżewska *et al.* 1999), fundamentally because in strict Stokes flow, there is no surface contact in finite time (Brady & Bossis 1988; Claeys & Brady 1989, 1993). A recent study by Li *et al.* (2024) shows that fibres passing over a triangular obstacle can show net displacements in Stokes transport flow even when not experiencing direct contact. The fibres are extended,

https://doi.org/10.1017/jfm.2026.11358 Published online by Cambridge University Press

non-spherical objects and their interactions with obstacles are modelled by effective forces (Dance *et al.* 2004), leaving open the question as to whether rigorously described hydrodynamic interactions can cause net displacement. Very recent work by Liu, Das & Hilgenfeldt (2025) describes particle motion in internal (vortical) Stokes flow and finds that purely hydrodynamic interactions with confining channel walls can indeed result in lasting displacements through repeated wall encounters. Such vortex flows have, however, not been practically implemented yet for this purpose. The present work, by contrast, aims at a rigorous hydrodynamic description of particle motion in Stokes flow external to an obstacle (the elementary process of DLD), establishing the required geometry of flow and obstacle to effect a lasting displacement, as well as bounds on its magnitude.

2. Hydrodynamic formalism of particle–wall interaction in Stokes flow

Microparticles placed in a background Stokes flow around an interface experience forces at varying distances from the boundary. Even at large distances (in bulk flow), particle trajectories deviate from the background flow because of Faxén's correction (Happel & Brenner 1965), but close to the interfaces, the hydrodynamic interaction between boundaries is dominant.

Different situations can be addressed in the modelling of particles in Stokes flow (Brenner 1961; Goldman *et al.* 1967*a*,*b*), particularly (i) the forces on a particle moving at a given speed, (ii) the forces on a particle held fixed in a certain location or (iii) the motion of a force-free particle. The present work focuses on the third scenario, which is particularly relevant for density-matched particles (absent the effects of gravity) in microfluidic devices. Setting thus the total force on the particle to zero, we quantify the modification of the particle velocity due to the effects of nearby boundaries altering particle motion in both the wall-parallel and the wall-normal directions.

A detailed analysis of the motion of force-free particles with wall-normal velocity corrections has been provided by Rallabandi *et al.* (2017). Other work has described wall-parallel velocity corrections far from and close to the wall (Ekiel-Jeżewska & Wajnryb 2006; Pasol *et al.* 2011). In our very recent study on particle motion in internal Stokes flow (Liu *et al.* 2025), we have constructed uniformly valid expressions for all particle–wall distances from this precursor work. Here, we extend the formalism to determine particle trajectories transported over an obstacle, representing a boundary whose orientation and curvature near the particle both change as the particle moves.

2.1. *Problem set-up*

Reflecting common situations in microfluidic set-ups with structures that span the entire height of a channel, we here describe two-dimensional Stokes flows $\boldsymbol{u}(\boldsymbol{x})$ in a Cartesian coordinate system $\boldsymbol{x} = (x, y)$. Although any two-dimensional Stokes flow around an obstacle is subject to the Oseen paradox (Proudman & Pearson 1957) and does not exist as a consistent solution to arbitrary distance from the obstacle wall, a unique background Stokes flow exists in the vicinity of the obstacle, and the range and accuracy of that solution can be arbitrarily increased by lowering the Reynolds number. We place a spherical, force-free inertialess particle in such a flow $\boldsymbol{u}(\boldsymbol{x})$ as sketched in figure 1(*a*).

We consider particle radii a_p much smaller than the radius of curvature of the obstacle wall $R(\boldsymbol{x})$. The unit vector $\boldsymbol{e}_\perp(\boldsymbol{x}_p)$ normal to the wall pointing towards the particle centre $\boldsymbol{x}_p$ defines the closest distance $h(\boldsymbol{x}_p)$ between particle centre and boundary. Tracking the particle trajectory under the influence of the obstacle needs careful modelling of the corrections to both the wall-parallel and the wall-normal velocity components of the particle particularly close to the obstacle, where the effects are most prominent.

https://doi.org/10.1017/jfm.2026.11358 Published online by Cambridge University Press

In such proximity, we have verified that effects of finite obstacle curvature (quantified in Rallabandi *et al.* (2017)) are small and do not alter the outcomes presented here (see Appendix D for details), so that we restrict ourselves to the flat-wall approximation ($a_p/R \to 0$) here.

Far from any walls, the motion of a spherical, neutrally buoyant particle is described by

$$\boldsymbol{v}_{p,far} = \boldsymbol{u}(\boldsymbol{x}_p(t)) + \boldsymbol{u}_{Faxen}(\boldsymbol{x}_p(t)), \tag{2.1}$$

with the effect of streamline curvature on the length scale of the particle size addressed by the Faxén correction:

$$\boldsymbol{u}_{Faxen}(\boldsymbol{x}) = \frac{a_p^2}{6}\nabla^2\boldsymbol{u}(\boldsymbol{x}). \tag{2.2}$$

The presence of an obstacle imposes wall effects, and thus an additional velocity correction, $\boldsymbol{W}$. With no inertia, the particle equation of motion remains a first-order dynamical system:

$$\frac{\mathrm{d}\boldsymbol{x}_p(t)}{\mathrm{d}t} = \boldsymbol{v}_p(\boldsymbol{x}_p(t)) = \boldsymbol{u}(\boldsymbol{x}_p(t)) + \boldsymbol{u}_{Faxen}(\boldsymbol{x}_p(t)) + \boldsymbol{W}(\boldsymbol{x}_p(t)). \tag{2.3}$$

In the far-field limit, $\boldsymbol{W}$ must decay to zero, leaving only the Faxén correction in effect. Decomposing the ambient velocity field $\boldsymbol{u} = u_{||}\boldsymbol{e}_{||} + u_\perp\boldsymbol{e}_\perp$ in the wall-parallel and wall-normal directions, we write

$$\boldsymbol{v}_{p||} = \left(\boldsymbol{u} + \frac{a_p^2}{6}\nabla^2\boldsymbol{u}\right)\cdot\boldsymbol{e}_{||} + W_{||}, \tag{2.4}$$

$$\boldsymbol{v}_{p\perp} = \left(\boldsymbol{u} + \frac{a_p^2}{6}\nabla^2\boldsymbol{u}\right)\cdot\boldsymbol{e}_\perp + W_\perp, \tag{2.5}$$

and quantify in the following the particle velocity corrections parallel to ($W_{||}$) and normal to ($W_\perp$) the wall. While we largely quote results from previous work (Liu *et al.* 2025), we point out where the present problem requires particular care and greater modelling effort.

2.2. *Wall-parallel corrections to the particle velocity*

The components of $\boldsymbol{W}(\boldsymbol{x}_p)$ depend on the wall distance, conveniently described by the dimensionless parameter

$$\Delta = \frac{h(\boldsymbol{x}_p) - a_p}{a_p}, \tag{2.6}$$

which is the surface-to-surface distance relative to the particle radius (Rallabandi *et al.* 2017; Thameem *et al.* 2017; Agarwal *et al.* 2018). The wall-parallel velocity correction $W_{||}$ slows down the wall-parallel velocity of a force-free particle by a fraction $f(\Delta)$, so that (2.4) takes the form

$$v_{p||}(x_p, y_p) = \left[(1 - f(\Delta))\left(\boldsymbol{u} + \frac{a_p^2}{6}\nabla^2\boldsymbol{u}\right)\cdot\boldsymbol{e}_{||}\right]_{\boldsymbol{x}_p}. \tag{2.7}$$

A uniformly valid expression for $f(\Delta)$ was obtained in Liu *et al.* (2025) by systematic asymptotic matching of results from Goldman *et al.* (1967*b*) for $\Delta \gg 1$ and Williams, Koch & Giddings (1992) for $\Delta \ll 1$ (including the lubrication limit), and is reproduced in Appendix A.

https://doi.org/10.1017/jfm.2026.11358 Published online by Cambridge University Press

2.3. *Wall-normal corrections to the particle velocity*

Employing a quadratic expansion of the background flow about the spherical particle's centre, a general expression for the normal component of the hydrodynamic force on a spherical, neutrally buoyant particle was obtained by Rallabandi *et al.* (2017). In the case of a force-free particle of interest here, this yields the wall-normal correction $W_\perp$ and thus the particle wall-normal velocity:

$$v_{p\perp}^{PE}(x_p, y_p) = \left[\left\{\boldsymbol{u} + \frac{a_p^2}{6}\nabla^2\boldsymbol{u} - a_p\frac{\mathcal{B}}{\mathcal{A}}(\boldsymbol{e}_\perp\cdot\nabla\boldsymbol{u}) + \frac{a_p^2}{2}\frac{\mathcal{C}}{\mathcal{A}}(\boldsymbol{e}_\perp\boldsymbol{e}_\perp : \nabla\nabla\boldsymbol{u}) + \frac{a_p^2}{2}\left(\frac{\mathcal{D}}{\mathcal{A}} - \frac{1}{3}\right)\nabla^2\boldsymbol{u}\right\}\cdot\boldsymbol{e}_\perp\right]_{\boldsymbol{x}_p}. \tag{2.8}$$

The full analytical expressions for the Δ-dependent functions $\mathcal{A}$, $\mathcal{B}$, $\mathcal{C}$ and $\mathcal{D}$ are provided in Rallabandi *et al.* (2017). For arbitrarily large separations ($\Delta\to\infty$), $\mathcal{B}/\mathcal{A}\to 0$, $\mathcal{C}/\mathcal{A}\to 0$ and $\mathcal{D}/\mathcal{A}\to 1/3$, so that $W_\perp\to 0$. We use the superscript PE ('particle expansion') to emphasise that all background flow velocities and derivatives are evaluated at $\boldsymbol{x}_p$.

As the particle approaches the wall ($\Delta\ll 1$) this particle expansion formalism becomes inaccurate – note that (2.8) is not guaranteed to vanish when the particle touches the wall ($\Delta = 0$). If instead we employ Taylor expansion of the background flow field $\boldsymbol{u}(\boldsymbol{x})$ around the point on the wall closest to the particle,

$$\boldsymbol{x}_w = \boldsymbol{x}_p - a_p\boldsymbol{e}_\perp(\boldsymbol{x}_p), \tag{2.9}$$

as suggested by Rallabandi *et al.* (2017), the no-penetration condition is enforced ('wall expansion'). The resulting particle velocity is linear in Δ to leading order:

$$v_{p\perp}^{WE} = 1.6147a_p^2\kappa(\boldsymbol{x}_p)\Delta + O(\Delta^2). \tag{2.10}$$

Here $\kappa(\boldsymbol{x}_p) = \partial_\perp^2 u_\perp(\boldsymbol{x}_w)$ is the background flow curvature at the wall point $\boldsymbol{x}_w$ from (2.9). Although (2.10) accurately determines the particle wall-normal velocity for $\Delta\ll 1$, we find that it does not smoothly transition to (2.8) when $\Delta\sim 1$. We therefore generalise and refine the wall-expansion procedure in this intermediate region by constructing second-order expansions of $\boldsymbol{u}(\boldsymbol{x})$ around variable expansion points $\boldsymbol{x}_E = \boldsymbol{x}_E(\boldsymbol{x}_p)$, i.e.

$$\boldsymbol{u}^{VE}(\boldsymbol{x}) = \boldsymbol{u}|_{\boldsymbol{x}=\boldsymbol{x}_E} + (\boldsymbol{x}-\boldsymbol{x}_E)\cdot(\nabla\boldsymbol{u})_{\boldsymbol{x}=\boldsymbol{x}_E} + \frac{1}{2}(\boldsymbol{x}-\boldsymbol{x}_E)(\boldsymbol{x}-\boldsymbol{x}_E) : (\nabla\nabla\boldsymbol{u})_{\boldsymbol{x}=\boldsymbol{x}_E}. \tag{2.11}$$

Replacing $\boldsymbol{u}$ by $\boldsymbol{u}^{VE}$ in (2.8) gives the generalised expression

$$v_{p\perp}^{VE}(x_p, y_p) = \left[\left\{\boldsymbol{u}^{VE} + \frac{a_p^2}{6}\nabla^2\boldsymbol{u}^{VE} - a_p\frac{\mathcal{B}}{\mathcal{A}}\left(\boldsymbol{e}_\perp\cdot\nabla\boldsymbol{u}^{VE}\right) + \frac{a_p^2}{2}\frac{\mathcal{C}}{\mathcal{A}}\left(\boldsymbol{e}_\perp\boldsymbol{e}_\perp : \nabla\nabla\boldsymbol{u}^{VE}\right) + \frac{a_p^2}{2}\left(\frac{\mathcal{D}}{\mathcal{A}} - \frac{1}{3}\right)\nabla^2\boldsymbol{u}^{VE}\right\}\cdot\boldsymbol{e}_\perp\right]_{\boldsymbol{x}_p}, \tag{2.12}$$

where the derivatives and resistance coefficients are still evaluated at the particle centre.

The functional form of the expansion point $\boldsymbol{x}_E(\boldsymbol{x}_p)$ is constructed for (2.12) to obey the WE and PE limits, i.e $\boldsymbol{x}_E\to\boldsymbol{x}_w$ for touching particles ($\Delta\to 0$) and $\boldsymbol{x}_E = \boldsymbol{x}_p$ for all $\Delta\geqslant\Delta_E$. For simplicity, we choose the linear relation

$$\boldsymbol{x}_E = \boldsymbol{x}_p - a_p\left(1 - \frac{\Delta}{\Delta_E}\right)\boldsymbol{e}_\perp \tag{2.13}$$

https://doi.org/10.1017/jfm.2026.11358 Published online by Cambridge University Press

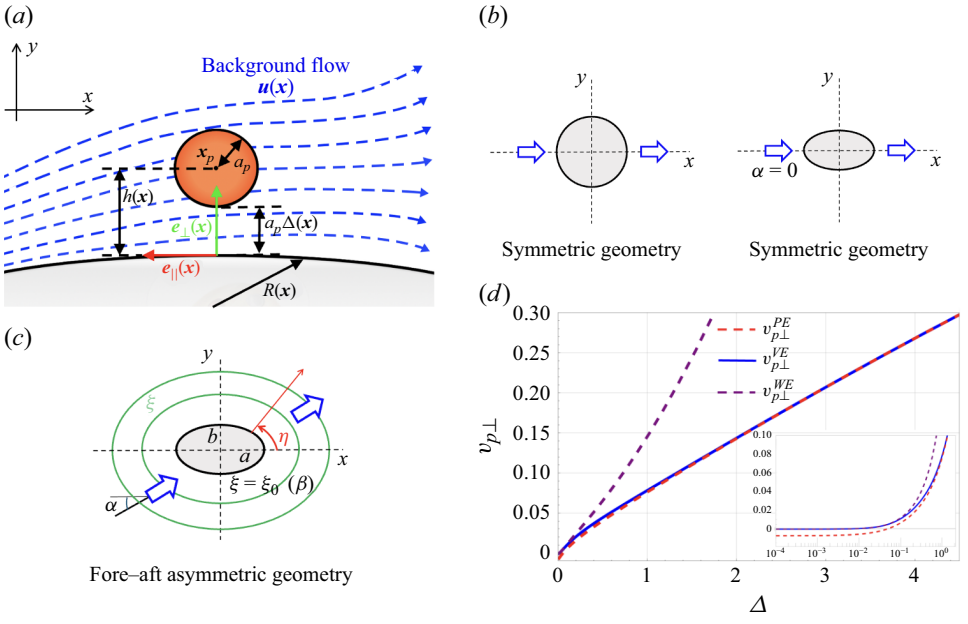


Figure 1. (*a*) Schematic of a small spherical particle of radius a_p located at $\boldsymbol{x}_p = (x_p, y_p)$ in the vicinity of an obstacle boundary of radius of curvature $R(\boldsymbol{x})$. The particle is immersed in a density-matched Stokes background flow $\boldsymbol{u}(\boldsymbol{x})$. (*b*) Sketches of fore–aft symmetric obstacle–flow geometries with a circular cylinder or a symmetrically placed elliptic cylinder. This fore–aft symmetry breaks in (*c*), where the flow has non-trivial angle of attack α. Also sketched is the elliptic coordinate system (ξ, η). (*d*) An example of wall-normal particle velocity as a function of the gap coordinate Δ at an angular position $\eta = 20°$ using variable expansion modelling (cf. (2.12)) with $\Delta_E = 3$ showing a smooth transition to the particle expansion for large $\Delta \gtrsim 1$ and to the wall expansion (inset) for $\Delta \ll 1$.

for $\Delta \leqslant \Delta_E$ and $\boldsymbol{x}_E = \boldsymbol{x}_p$ otherwise. Here, Δ_E denotes a specific choice of Δ that ensures a smooth interpolation between $v_{p\perp}^{WE}$ and $v_{p\perp}^{PE}$ as shown in figure 1(*d*) for $\Delta_E = 3$. We adopt this choice for subsequent sections, while carefully checking that the results are robust against other $\mathcal{O}(1)$ choices of Δ_E (Appendix C).

Using (2.7) and (2.12) in the dynamical system (2.3) constitutes our formalism for computing particle motion in the presence of wall effects for arbitrary Stokes background flow.

3. Symmetry-breaking inertialess transport around an obstacle

We apply the modelling detailed above to particles transported towards and past an obstacle. If a particle's approach to and departure from the interface on its trajectory occur in a symmetric fashion, the gradients normal to the wall cancel out during approach and departure, so that no net displacement (relative to the streamline on which the particle starts) will be observed. This is clearly the case for a single circular cylinder obstacle (figure 1*b*). However, if the combined geometry of the boundary and the flow field breaks this symmetry, net displacement and thus meaningful manipulation of particle transport are possible. We investigate here the case of an elliptic cylinder obstacle with aspect ratio $\beta = b/a$ (with a and b the major and minor axes, respectively) placed in a uniform Stokes flow U whose direction makes an angle α with the major axis. This situation is shown in figure 1(*c*) together with associated Cartesian and elliptic coordinate systems. Note that symmetry arguments again preclude net displacement if $\alpha = 0$ or $\alpha = \pi/2$ (figure 1*b*).

https://doi.org/10.1017/jfm.2026.11358 Published online by Cambridge University Press

We use the single elliptic obstacle as the simplest case study of fore–aft symmetry breaking, which in traditional DLD set-ups is achieved by inclining a forest of circular pillars relative to the uniform stream. The Stokes background flow around the elliptic cylinder is known analytically as a solution to the biharmonic equation $\nabla^4\tilde{\psi}_B = 0$ for the streamfunction $\tilde{\psi}_B$. We choose the semimajor axis a and the uniform flow speed U as our length and velocity scales, so that $\tilde{\psi}_B$ is non-dimensionalised by aU.

The Oseen paradox restricts this solution to an inner region in the vicinity of the obstacle surface. It is implicit in the work of Berry & Swain (1923) and was explicitly derived by Shintani, Umemura & Takano (1983) in elliptic coordinates (ξ, η) as the infinite sum $\tilde{\psi}_B = \sum_{n=1}^{\infty} \tilde{\psi}_n$ with

$$\begin{aligned}\tilde{\psi}_n = \frac{1}{(\ln Re)^n}\big[&\Lambda_n\big\{(\xi-\xi_0)\cosh\xi + \sinh\xi_0\cosh\xi_0\cosh\xi - \cosh^2\xi_0\sinh\xi\big\}\cos\eta \\ &- \Omega_n\big\{(\xi-\xi_0)\sinh\xi - \sinh\xi_0\cosh\xi_0\sinh\xi + \sinh^2\xi_0\cosh\xi\big\}\sin\eta\big].\end{aligned} \tag{3.1}$$

Here $x = \sqrt{1-\beta^2}\cosh\xi\cos\eta$ and $y = \sqrt{1-\beta^2}\sinh\xi\sin\eta$ relate Cartesian and elliptic coordinates, and $\xi = \xi_0 = (1/2)\ln[(1+\beta)/(1-\beta)]$ defines the elliptic cylinder surface. The prefactors Λ_n and Ω_n are functions of α and β obtained from asymptotic matching (Kaplun 1957; Proudman & Pearson 1957). The analytical form of (3.1), by construction, does not contain fluid inertia except an implicit dependence on Reynolds number Re which defines the Oseen distance – the range of validity of the solution around the obstacle which is $1/Re$ (Proudman & Pearson 1957; Batchelor 2000), and can be made arbitrarily large by choosing a very small Re. Since our goal is to investigate the wall effect on particle trajectory and effective particle–wall interaction always occurs in the proximity of the obstacle, this flow description reflects reality to a well-defined degree of accuracy. In the limit $Re \to 0$, the $n = 1$ term of (3.1) is dominant, and we scale out the Re dependence by defining the rescaled background flow as

$$\begin{aligned}\psi_B &= (-\ln Re)\tilde{\psi}_{n=1} \\ &= \Lambda_1\big\{(\xi-\xi_0)\cosh\xi + \sinh\xi_0\cosh\xi_0\cosh\xi - \cosh^2\xi_0\sinh\xi\big\}\cos\eta \\ &\quad - \Omega_1\big\{(\xi-\xi_0)\sinh\xi - \sinh\xi_0\cosh\xi_0\sinh\xi + \sinh^2\xi_0\cosh\xi\big\}\sin\eta,\end{aligned} \tag{3.2}$$

with $(\Lambda_1, \Omega_1) = \sqrt{1-\beta^2}(\sin\alpha, \cos\alpha)$. This analytical expression agrees with the description of Stokes flow over an inclined elliptic fibre by Raynor (2002). It could be improved in accuracy by taking into account terms of higher n successively smaller by powers of $1/|\ln Re|$, but we take (3.2) to allow for clearer analytical scaling results. Figure 2(*a*) shows streamline contours (ψ_B) for an angle of attack $\alpha = 30°$ and obstacle aspect ratio $\beta = 0.5$. Lastly, in order to isolate and explicitly quantify the wall effect on particle motion only, we use as our reference streamfunction the sum of ψ_B and the Faxén streamfunction $\psi_{Faxen} = a_p^2/6\nabla^2\psi_B$, i.e.

$$\psi = \psi_B + \psi_{Faxen}. \tag{3.3}$$

We have confirmed (see Appendix B) that particle displacement effects from the Faxén correction are negligible compared with those from particle–wall interaction at small Δ, while they are absolutely small when $\Delta \gg 1$ and thus do not affect our findings on net displacement resulting from particle–obstacle encounters.

https://doi.org/10.1017/jfm.2026.11358 Published online by Cambridge University Press

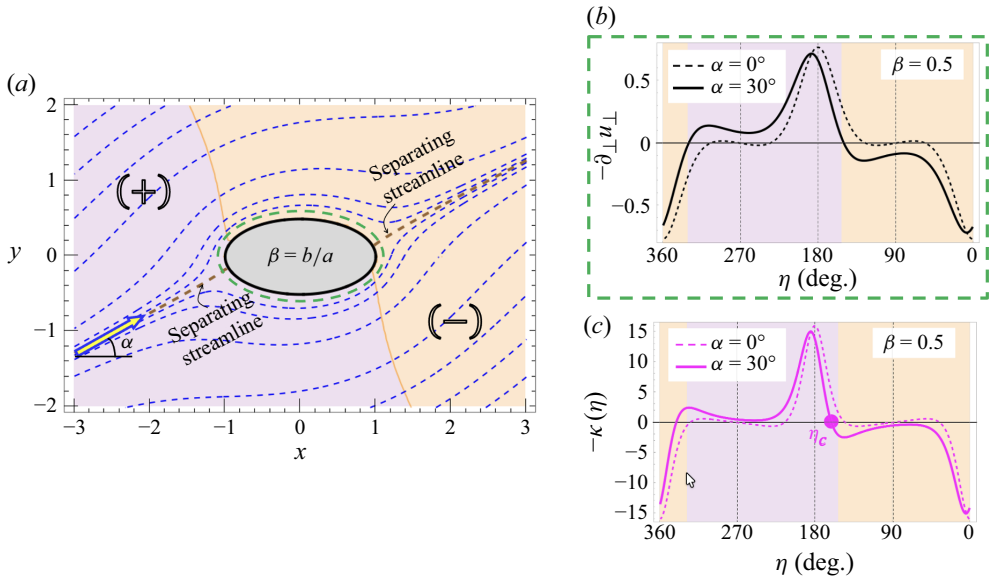


Figure 2. (*a*) Fore–aft asymmetric Stokes flow (dashed blue streamline contours from (3.2)) impacting on an elliptic obstacle ($\beta = 1/2$) under an inclination $\alpha = 30°$. Here $W_\perp$ is positive in the purple shaded zone and is negative in the orange shaded zone indicating particle repulsion from the obstacle and attraction towards the obstacle, respectively. The separating streamlines $\psi = 0$ are indicated in dashed brown. (*b*) The sign changes of the quantity $\partial_\perp u_\perp$ reflect, to leading order, those of $W_\perp$ (shading). This quantity is measured along the green dashed line in (*a*), locations at a distance $\Delta = 1$, here for $a_p = 0.1$, where $\partial_\perp u_\perp$ dominates the corrections of particle motion. (*c*) The background flow curvature $-\kappa = -\partial_\perp^2 u_\perp$ evaluated at the obstacle wall determines normal particle motion in the wall expansion model (2.10) for $\Delta \ll 1$. The upstream zero of this quantity, η_c, indicates a point of closest approach to the obstacle as discussed in § 4.3.

4. Results and discussion

The hydrodynamic formalism of § 2 is now applied to compute the particle trajectory of transport around an elliptic obstacle in the inertialess flow ψ from (3.3). The equations of motion (2.7) and (2.12) use the background flow velocity $\boldsymbol{u}$ derived from ψ in (3.2) via $u_\eta(\xi,\eta) = -g\,\partial_\xi \psi_B$, $u_\xi(\xi,\eta) = g\,\partial_\eta \psi_B$, where $g = g(\xi,\eta) = [(1-\beta^2)(\cosh^2\xi - \cos^2\eta)]^{-1/2}$ is the scale factor of the elliptic coordinate system (Shintani *et al.* 1983; Raynor 2002). For numerical computations, we transform all equations into Cartesian reference coordinates, while for some analytical arguments, we use elliptic coordinates directly.

Qualitatively, the particle is transported towards the obstacle surface on the upstream side and away from it on the downstream side. If the initial position of the particle leads to a very close approach to the obstacle wall (or even a hypothetical overlap with passive transport), $W_\perp$ will act to repel the particle from the wall on the upstream side. Conversely, $W_\perp$ represents an attraction downstream. Figure 2(*a*) confirms these observations and shows that for non-trivial α, β the zones of repulsion and attraction are strongly asymmetric.

We will be most interested in particle trajectories that follow the obstacle outline closely, i.e. where Δ is not large. It can be verified that at $\Delta \sim 1$, the magnitude of $W_\perp$ is dominated by the first normal derivative term $-a_p(\mathcal{B}/\mathcal{A})\partial_\perp u_\perp$ in (2.8). Indeed, figure 2(*b*) confirms that the sign of $-\partial_\perp u_\perp$ determines total attraction ($-$) or repulsion ($+$) to good accuracy for points at a distance of $h = 2a_p$ from the wall ($\Delta = 1$).

https://doi.org/10.1017/jfm.2026.11358 Published online by Cambridge University Press

In the limit $\Delta \to 0$, the net effect of $W_\perp$ on the particle motion is determined to leading order of Δ by the wall flow curvature $\kappa = \partial_\perp^2 u_\perp$ (cf. (2.10)). Figure 2(*c*) demonstrates that κ changes sign in very similar angular positions as the full $W_\perp$. We focus on information about $W_\perp$ here, as its effect dominates particle streamline crossing, while $W_\parallel$ mainly serves to slow down particles on their path.

We illustrate particle trajectories and displacements in the following with particles that travel from left to right 'above' the obstacle, where the repulsion region (+), encountered first, is shorter than the attraction region (−). All behaviour of particles travelling 'below' the obstacle can be inferred by symmetry as discussed later. The cases 'above' and 'below' have two separating streamlines ($\psi = 0$) as boundaries, representing a remaining flow symmetry: because of time reversibility of the Stokes flow (and the resulting hydrodynamic effects, which are linear in the Stokes flow), no particle can cross over these separating streamlines, which intersect the obstacle at the angular coordinate $\eta^{sep} = \arctan(\beta \tan\alpha)$ downstream and $\pi + \eta^{sep}$ upstream, respectively.

4.1. *Particle trajectories with net displacement*

The equation of motion of the particle is solved numerically to obtain the trajectory $\boldsymbol{x_p}(t)$. We define a complete journey of a particle from left to right as starting from an initial $x = x_i$ position and ending at $x_f = -x_i$ position. It is important to note that:

(i) The inherent linearity in Stokes flow causes the wall effects $\boldsymbol{W}$ to be fully time-reversible, meaning that particles will come back exactly to their starting points in reversing the flow.
(ii) Stokes flow does not possess any memory from inertia. Thus, the effect on the particle trajectory by $\boldsymbol{W}$ is instantaneous, and an initial particle position determines the full trajectory.
(iii) Because of the anti-symmetry of the flow about the separating streamlines, a trajectory transported above the obstacle from an initial streamfunction value $\psi = \psi_i$ is equivalent to a trajectory starting at $\psi = -\psi_i$ that is transported below in the opposite direction.

For empirical computations, unless otherwise stated, we choose $a_p = 0.1$ and track the particle centre positions to get pathlines. Two representative trajectories are shown in figure 3(*a*): one (in orange) never gets close to the obstacle (as $\Delta > 1$ throughout), while the other particle (in red) spends the majority of time creeping around the obstacle at very small gap values ($\Delta \ll 1$), a trajectory called a 'dive' in porous media literature (Miele *et al.* 2025). Figure 3(*c*) shows the dynamics of the gap Δ. The inset magnifies the closest approach of the dive trajectory towards the wall (position C), and verifies that the dynamics there is closely approximated by the leading-order wall expansion model (2.10).

With an initial condition far from the obstacle (a situation common in microfluidics devices; we take $x_i = -5$, although results are insensitive to this choice), at first the particle moves along its initial streamline $\psi = \psi_i$ (stage (1) in figure 3). When closer to the obstacle, the wall-normal correction counteracts the background flow still pointing towards the obstacle. At position C, the normal flow velocity $u_\perp$ and the wall effect $W_\perp$ cancel, so that the particle normal velocity $v_{p\perp} = 0$ and the particle–obstacle gap Δ reaches its minimum Δ_{min} (figure 3*c*).

Proceeding further in the dive stage (2), the wall effect $W_\perp$ becomes negative (cf. Figures 2*b* and 2*c*) and thus pushes the particle towards the obstacle while the background flow causes transport away from the wall. This continues until the particle ends its travel

https://doi.org/10.1017/jfm.2026.11358 Published online by Cambridge University Press

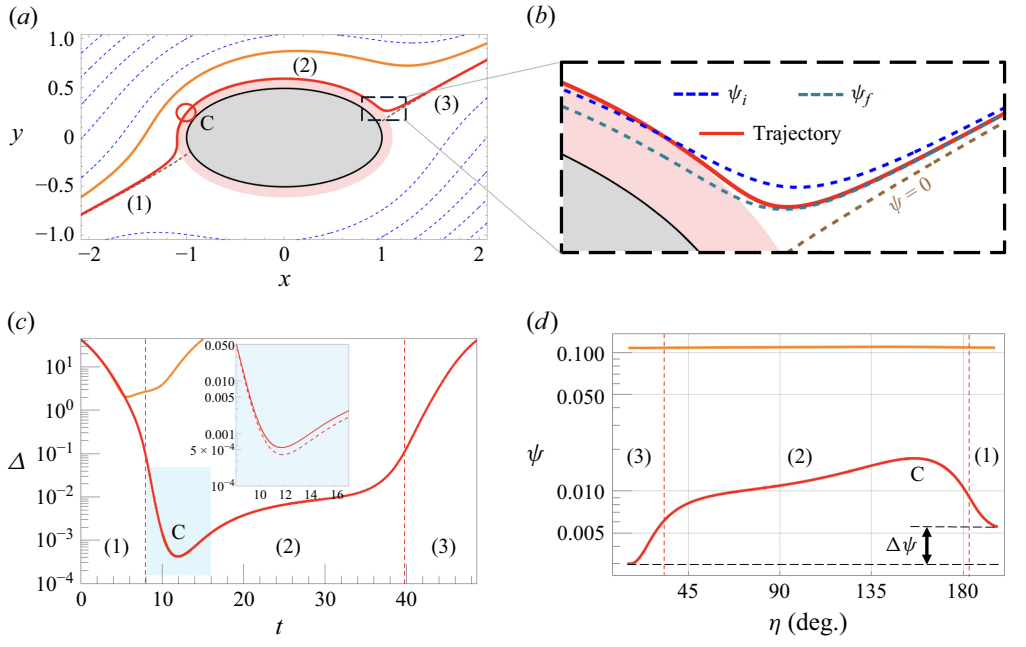


Figure 3. (*a*) Two computed trajectories (orange and red) of an $a_p = 0.1$ particle above an obstacle ($\beta = 0.5$) and $\alpha = 30°$ inclined Stokes flow (ψ isolines in dashed blue). Red shading indicates the exclusion zone for the hard-sphere particle centre. (*b*) Magnified downstream view shows that the final streamline the particle asymptotes to is lower than its initial streamline ($\psi_f < \psi_i$). (*c*) Particle–wall gap Δ as a function of travel time. The orange trajectory stays far from the wall ($\Delta > 1$), while the red trajectory remains very close ($\Delta \ll 1$). The inset shows good agreement around the minimum with computations using the wall expansion model (2.10) (red dashed line). (*d*) Local value of streamfunction on the trajectories as a function of angular position η. The orange trajectory remains essentially undeflected, while the red trajectory shows the effects of strong deflection away (1–2) and towards (2–3) the obstacle. Asymmetry of the flow ensures a net change in streamfunction $\Delta\psi = |\psi_f - \psi_i|$.

downstream on a well-defined final streamline $\psi = \psi_f$ (stage (3) in figure 3). For the situation depicted here ($\alpha < \pi/2$), we see that the phase of inward pull is of greater extent than that of outward repulsion, and that indeed there is a net downward displacement of the particle ($\psi_f < \psi_i$; see figure 3*b*).

It is convenient to quantify displacements by changes of the instantaneous streamfunction value of the particle position. Figure 3(*d*) shows ψ as a function of angular elliptic coordinate η. While the trajectory staying far from the obstacle (orange) shows negligible changes, the dive trajectory (red, very small ψ_i) registers a rapid increase of ψ in the dive phase up to C, and then a gradual decrease to a lasting displacement with well-defined $\Delta\psi = |\psi_f - \psi_i|$, which quantifies the strength of net deflection due to the symmetry-broken flow geometry.

At first glance, this implies larger $\Delta\psi$ as ψ_i decreases. However, when the initial position approaches the separating streamline $\psi_i \to 0$, this tendency cannot continue: particles cannot cross the separating streamline for symmetry reasons (see above), so $\psi_f \to 0$ is required and also the (downward) deflection must vanish, $\Delta\psi \to 0$. This reasoning guarantees a characteristic maximum value of net displacement $\Delta\psi$ for a particular ψ_i. In the following subsections we systematically describe this surprising effect both numerically and analytically.

https://doi.org/10.1017/jfm.2026.11358 Published online by Cambridge University Press

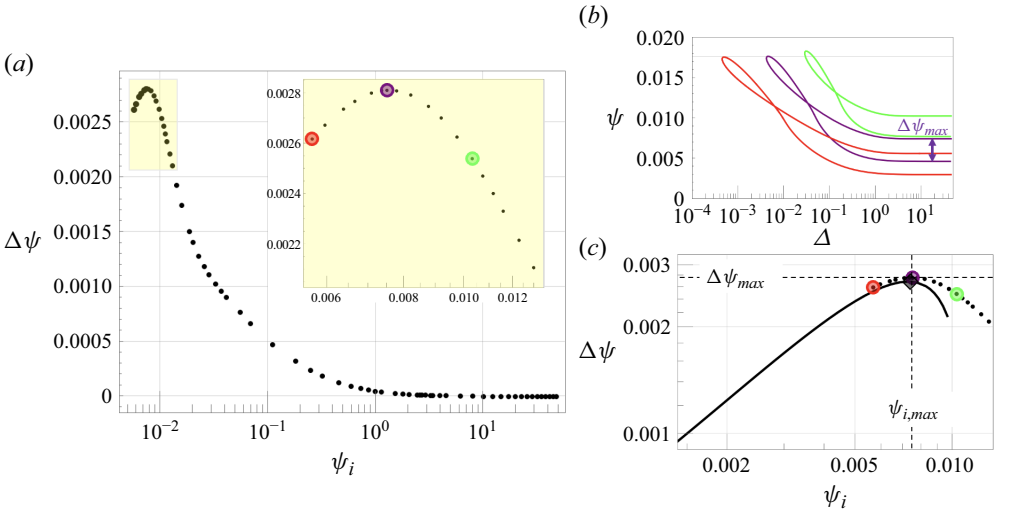


Figure 4. Particle net displacement results for $(\alpha, \beta, a_p) = (30°, 0.5, 0.1)$. (*a*) Plot of displacement $\Delta\psi$ for particle trajectories released from different initial streamlines ψ_i. The inset magnifies the region around the maximum value $\Delta\psi_{max}$. (*b*) Variation of ψ with Δ along the trajectories corresponding to the coloured points in (*a*), including the $\Delta\psi_{max}$ trajectory in purple. (*c*) The solid line depicts $\Delta\psi(\psi_i)$ from the analytical model (4.5) for small ψ_i. Both the magnitude of $\Delta\psi_{max}$ and its location $\psi_{i,max}$ are in good agreement with the empirical calculations.

4.2. *Analysis of net displacements*

4.2.1. *Integrating the dynamical system*

Numerical integration of the particle trajectory was performed as described in § 2 for varying initial conditions. We fix $x_i = -5$ and vary y_i in $\psi_i = \psi(x_i, y_i)$. The final streamfunction value is then assessed as $\psi_f = \psi(-x_i, y_f)$ when the particle's x position reaches $x_p = -x_i$. We choose $|x_i|$ large enough that it does not influence the result, i.e. changes in ψ for particle positions $x < x_i$ or $x > x_f$ are negligible.

Figure 4(*a*) shows the variation of the deflection measure $\Delta\psi$ with ψ_i for $\beta = 1/2$, $\alpha = 30°$. Particles that start far away from the separating streamline ($\psi_i \gtrsim 1$) experience minimal wall interaction throughout and $\Delta\psi$ remains nearly zero. Particles accumulate meaningful wall effect, and thus net displacement, as they encounter the obstacle in $\Delta < 1$ when starting at smaller ψ_i. The computations confirm the general argument above, showing a prominent maximum in $\Delta\psi$ at a small value of ψ_i. The inset highlights three initial conditions before (green), at (purple) and beyond (red) the maximum. In figure 4(*b*) we show the changes in ψ and Δ on these three particle trajectories.

The dynamical system is solved in Mathematica with controlled accuracy, which for initial positions $\psi_i \lesssim 0.005$ become computationally too demanding. The maximum in $\Delta\psi$ is, however, well resolved and we show below that we can understand the behaviour for $\psi_i \to 0$ analytically. The value of the maximum, $\Delta\psi_{max}$, and the corresponding initial position $\psi_{i,max}$ are main results of the current work that characterise the maximum net deflection that can be expected from a given symmetry-broken obstacle.

We stress that the streamfunction changes quantified here are with respect to the reference flow ψ from (3.3) and thus explicitly quantify wall effects only. The Faxén term in the reference flow describes the bulk flow curvature effects on particle trajectories (relative to passive transport in the background Stokes flow). We confirm in Appendix B

https://doi.org/10.1017/jfm.2026.11358 Published online by Cambridge University Press

that deflection by the Faxén term in the absence of the wall is at least one order of magnitude smaller than the wall effect, so that we isolate the main physics here.

4.2.2. *Analytical formalism*

In this section, we develop a method of predicting $\Delta\psi_{max}$, particularly in the limit $\psi_i \to 0$, which proves computationally challenging. We shall see that only information directly derived from the background flow field is needed.

All trajectories for $\psi_i \lesssim \psi_{i,max}$ are of the 'red' type in figure 3, i.e. they (1) approach the obstacle in close proximity of the upstream separating streamline (the angular particle position is $\eta_i \approx \pi + \eta^{sep}$), (2) accumulate meaningful deflection while moving along the obstacle surface maintaining very small gaps $\Delta \ll 1$ ('dives'; Miele *et al.* 2025) and (3) leave on a final streamline again close to the downstream separating streamline ($\eta_f \approx \eta^{sep}$). To good approximation, the important 'dive' phase is described by the wall expansion model (2.10) (see the inset of figure 3*c*). Noting $v_{p\perp} = a_p \mathrm{d}\Delta/\mathrm{d}t$, and dividing by $\mathrm{d}\eta/\mathrm{d}t$ along the trajectory, we write

$$\frac{\mathrm{d}(\log\Delta)}{\mathrm{d}\eta} = 1.6147\frac{a_p\kappa}{\mathrm{d}\eta/\mathrm{d}t}, \tag{4.1}$$

an equation we want to integrate from a starting point at the end of phase (1) (Δ_i, η_i) to an end point at the start of phase (3) (Δ_f, η_f). As particle displacements are strongly dominated by phase (2), the results are insensitive to the choice of Δ_i and Δ_f, as long as both are $\ll 1$. In particular, we can choose $\Delta_i = \Delta_f = \Delta^*$ and thus require

$$\int_{\eta_i}^{\eta_f} 1.6147\frac{a_p\kappa}{\mathrm{d}\eta/\mathrm{d}t}\mathrm{d}\eta = 0. \tag{4.2}$$

To make analytical progress, we observe that $\mathrm{d}\eta/\mathrm{d}t$ along the trajectory is the rate of change in the η direction of a particle moving at a distance of $\approx a_p$ from the obstacle surface, which translates to the wall-parallel particle velocity $v_{p\parallel}$, and further to the η component of the background velocity u_η as defined in § 4:

$$\begin{aligned}\frac{\mathrm{d}\eta}{\mathrm{d}t} &= g(\xi_{a_p},\eta)v_{p\parallel} = g(\xi_{a_p},\eta)(1-f(\Delta))u_\parallel = g(\xi_{a_p},\eta)(1-f(\Delta))u_\eta(\xi_{a_p},\eta)\\ &= -g^2(\xi_{a_p},\eta)(1-f(\Delta))\partial_\xi\psi_B(\xi_{a_p},\eta).\end{aligned} \tag{4.3}$$

These equations, accurate to relative $\mathcal{O}(a_p^2)$, contain the scale factor of the elliptic coordinate system $g = g(\xi,\eta)$ and the ξ derivative of the background streamfunction ψ_B (cf. §§ 3 and 4) both evaluated at $\xi_{a_p}(\eta) = \xi_0 + a_p g(\xi_0,\eta)$, representing points a distance a_p from the obstacle wall. The factor $f(\Delta)$ from (2.7) depends very weakly on Δ over the range of interest here, so that we replace it by a constant average value $\tilde{f} = \mathcal{O}(1)$. The choice of this constant $\tilde{f}$ is irrelevant for solving (4.2). Combining the constants into $\mathcal{S} = -1.6147/(1-\tilde{f})$, the integrand of (4.2) becomes

$$\phi(\eta) = \mathcal{S}\frac{a_p\kappa}{g^2\partial_\xi\psi_B}, \tag{4.4}$$

which is now entirely defined by the background flow, and is a function of η only. Its behaviour is discussed in more detail in Appendix E.

Introducing for convenience the indefinite integral $I(\eta) \equiv \int^\eta \phi(\tilde{\eta})\mathrm{d}\tilde{\eta}$, the condition (4.2) becomes

$$I(\eta_f) = I(\eta_i), \tag{4.5}$$

https://doi.org/10.1017/jfm.2026.11358 Published online by Cambridge University Press

relating valid pairs of initial and final η coordinates. These translate into initial and final streamfunction values:

$$\psi_i^* = \psi(\Delta = \Delta^*, \eta = \eta_i), \tag{4.6}$$

$$\psi_f^* = \psi(\Delta = \Delta^*, \eta = \eta_f). \tag{4.7}$$

The results of this calculation are insensitive to the precise value of Δ^* as long as it is $\ll 1$ (see Appendix C for a discussion). Figure 4(*c*) uses $\Delta^* = 0.05$ and shows good agreement with the small-ψ_i trajectory data from figure 4(*a*). It is remarkable that this small-ψ_i theory not only yields an asymptote for $\Delta\psi \to 0$, but also captures the position of $\Delta\psi_{max}$.

4.2.3. *Scaling laws for* $\Delta\psi_{max}$

The analytical approach in § 4.2.2 is successful, but still evaluates the necessary functions and integrals numerically. In order to understand systematically how maximum deflection depends on the parameters of the particle–obstacle encounter, we employ further simplifications. First, we replace ψ by ψ_B in the definition of $\Delta\psi$ (cf. (3.2)), again using $\xi = \xi_{a_p}$, and furthermore expand ψ_B in small $\xi - \xi_0$ (these approximations are consistent with $a_p \ll 1$).

To leading order in a_p, the simplified background streamfunction reads

$$\hat{\psi}_B(\eta) = (\sin\eta\cos\alpha - \beta\cos\eta\sin\alpha)a_p^2 g^2(\xi_0, \eta). \tag{4.8}$$

This streamfunction expression is used to evaluate initial and final values $\hat{\psi}_{i,f} = \hat{\psi}_B(\eta_{i,f})$ for given angular arguments, and also to obtain simplified versions of the functions $\phi \to \hat{\phi}$ from (4.4) and $I \to \hat{I}$ resulting in an algebraically simplified analogue of (4.5):

$$\hat{I}(\eta_f) = \hat{I}(\eta_i). \tag{4.9}$$

To directly compute the maximum of $\Delta\psi(\hat{\psi}_i)$, we need to derive a second equation. The monotonicity of $I(\eta)$ and $\psi(\eta)$ around $\Delta\psi_{max}$ (see Appendix E) allows us to first write the maximum condition as

$$\frac{\partial\Delta\psi}{\partial\hat{I}} = 0, \tag{4.10}$$

and further, defining $\zeta(\eta) \equiv \partial_\eta\hat{\psi}_B/\hat{\phi}$, we conclude that (4.10) implies

$$\zeta(\eta_f) = \zeta(\eta_i). \tag{4.11}$$

Solving (4.9) and (4.11) simultaneously yields a pair of values $(\eta_i, \eta_f) = (\eta_{i,max}, \eta_{f,max})$ that determine $\Delta\psi_{max}$ from $\psi_{i,max} = \hat{\psi}_B(\eta_{i,max})$ and $\psi_{f,max} = \hat{\psi}_B(\eta_{f,max})$. To make analytical progress, it is crucial to acknowledge that the upstream and downstream angular positions η_i and η_f are not equidistant from the separation streamlines, but that in writing $\eta_i = \pi + \eta^{sep} - \Delta\eta_i$ and $\eta_f = \eta^{sep} + \Delta\eta_f$, the angular deviations have a leading-order asymmetry $\delta = \Delta\eta_i - \Delta\eta_f$ (see Appendix E), which vanishes as $\alpha \to 0$. Consistent expansion in small α or equivalently in small $\sin 2\alpha$ yields the leading-order expressions $\delta = \delta_1 \sin 2\alpha$ and $\eta^{sep} = (\beta/2)\sin 2\alpha$. Substituting into (4.9), (4.11) and further expansion in the small quantities a_p and $\Delta\eta_f$ results in a system of two equations that can be solved for δ_1 and $\Delta\eta_f$ as detailed in Appendix E, yielding

$$\Delta\eta_f = \frac{a_p\beta^2\left[\left(2-\beta^2\right)E\left(1-\frac{1}{\beta^2}\right) - K\left(1-\frac{1}{\beta^2}\right)\right]}{\left(1-\beta^2\right)\left(6a_p+\beta^2\right)}, \tag{4.12}$$

https://doi.org/10.1017/jfm.2026.11358 Published online by Cambridge University Press

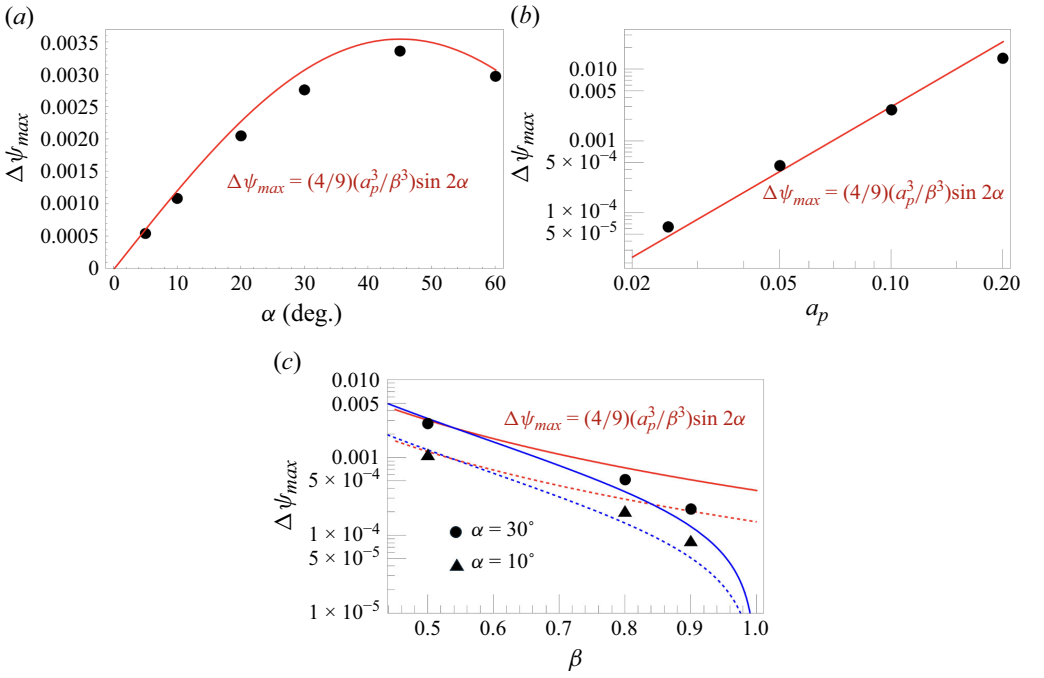


Figure 5. Scaling of $\Delta\psi_{max}$ with (*a*) flow angle α ($a_p = 0.1$, $\beta = 0.5$), (*b*) particle size a_p ($\alpha = 30°$, $\beta = 0.5$) and (*c*) aspect ratio β ($a_p = 0.1$, $\alpha = 10°$ and $30°$). The red lines are obtained from the analytical scaling theory (4.15) for $\beta \ll 1$. In (*c*), the small-β theory is successful even for $\beta = 0.5$, but to capture displacements for near-spherical obstacles ($\beta \lesssim 1$), the complete theory of (4.12)–(4.14) is needed (blue lines).

$$\delta_1 = \frac{6a_p^3\beta[(2-\beta^2)E(1-\frac{1}{\beta^2}) - K(1-\frac{1}{\beta^2})]^2}{(1-\beta^2)(6a_p+\beta^2)^2}. \tag{4.13}$$

Here K and E are the complete elliptic integrals of the first kind and second kind, respectively.

The same consistent expansions in $\hat{\psi}_B$ eventually provide an analytical expression for $\Delta\psi_{max}$ in terms of δ_1 and $\Delta\eta_f$, namely

$$\Delta\psi_{max} = a_p^2\left[\frac{\delta_1}{\beta^2} + \frac{2\left(1-\beta^2\right)}{\beta^3}\Delta\eta_f^2 + \delta_1\frac{\left(-6+5\beta^2\right)}{2\beta^4}\Delta\eta_f^2 + O\left(\Delta\eta_f^3\right)\right]\sin 2\alpha. \tag{4.14}$$

Plugging (4.12) and (4.13) into (4.14) allows for evaluation at arbitrary β values. For $\beta \ll 1$, this expression has a much simpler limit:

$$\Delta\psi_{max} = \frac{4}{9}\frac{a_p^3}{\beta^3}\sin 2\alpha \qquad (\beta \ll 1). \tag{4.15}$$

Remarkably, we find that for our preferred study case $\beta = 1/2$ the small-β solution (4.15) still reproduces trajectory data very accurately, as demonstrated by the red curves in figure 5. Figure 5(*a*,*b*) shows that (4.15) compares very well with direct trajectory calculations varying flow angle of attack α and particle size a_p. The expansions in small $\sin 2\alpha$, a_p and β behind the analytical expression maintain good accuracy beyond their strict limits: the leading-order angle dependence $\sin 2\alpha$ appears valid for all angles, and is indeed the expected dependence from the elliptic symmetry of the obstacle geometry.

https://doi.org/10.1017/jfm.2026.11358 Published online by Cambridge University Press

Particle sizes as large as $a_p = 0.2$ still yield good agreement. Figure 5(*c*) does find that approximating displacements around near-circular obstacles requires the full scaling theory (4.12)–(4.14), but the displacement effect is also dramatically smaller as $\beta \to 1$ and the obstacle fore–aft symmetry vanishes. The surprisingly strong β^{-3} dependence in (4.15), and its accuracy for $\beta = 1/2$, suggests that employing even slightly more eccentric obstacles could strongly enhance particle deflection. For much smaller β, however, effects of obstacle surface curvature on the hydrodynamic wall corrections ((D1) in Appendix D) will likely become important and modify the results.

4.2.4. *Particle size separation*

We now compare the impact on particle separation by size due to the hydrodynamic effects modelled here with that inferred from the detailed modelling of short-range roughness effects (Frechette & Drazer 2009). The present work treats interaction of a single particle and obstacle, and thus cannot provide critical particle sizes for crossing separating streamlines between multiple obstacles in a DLD array, but we can ask by how much the particle–obstacle interaction makes the trajectories of two particles of different sizes deviate from each other, setting up further downstream separation. We choose typical dimensional microparticle radii $a_{p1} = 4$ μm and $a_{p2} = 8$ μm, interacting with obstacles of circular cross-section with $r = 32$ μm. In Frechette & Drazer (2009), the obstacles are themselves spherical and the interaction depends weakly on the symmetry-breaking surface roughness – we assume an experimentally relevant scale of ∼100 nm (Smart & Leighton Jr 1989; Yang, Zhang & Hsu 2007; Hülagü *et al.* 2024). The results in Frechette & Drazer (2009) then allow for an evaluation of the displacements of the two particles when they are initially on the same streamline. Among all initial conditions, the maximum expected difference for the example parameters above is $\Delta n_{12} \approx 1.4$ μm perpendicular to the uniform flow direction. Evaluating by comparison the hydrodynamic effects of encountering an elliptic cylinder, we choose scales of $a = 40$ μm and $b = 20$ μm (resulting in nearly the same cross-sectional area as the circular obstacle), and a flow angle of attack $\alpha = 30°$. At a distance of $\sim a$ behind the obstacle, we find a maximal displacement difference of the same particle sizes normal to the far-field flow of $\Delta n_{12} \approx$ 0.9 μm. Thus, the short-range roughness interactions for symmetric obstacles and the hydrodynamic effects modelled here for symmetry-breaking obstacles have a comparable effect on particle separation by size. We emphasise here that our work does not invalidate the existing DLD explanation through non-hydrodynamic short-range interactions. Rather, we argue that both effects can naturally coexist and should both be taken into account when modelling DLD and when designing DLD devices, as we expect significant quantitative changes when obstacle cross-sections are made asymmetric.

4.3. *Closest approach and sticking*

Our formalism finds the strongest net deflections of particles when particles follow the obstacle surface very closely, i.e. $\Delta \ll 1$ along a significant part of the trajectory ('dives'; Miele *et al.* 2025). Necessarily, the minimum gap Δ_{min} on such trajectories becomes very small, and with typical microfluidic scales of obstacle and particle sizes, Δ_{min} can easily translate to submicrometre distances. In the presence of short-range attractive interactions between the surfaces (London forces, van der Waals attraction, etc.) this can lead to sticking (capture) of the particles, an effect important in fouling and cleaning (Rajendran *et al.* 2025; Kumar & Ismail 2015; Gul, Hruza & Yalcinkaya 2021), porous-media filtration (Miele *et al.* 2025; Mays & Hunt 2005) or elimination of pathogens

https://doi.org/10.1017/jfm.2026.11358 Published online by Cambridge University Press

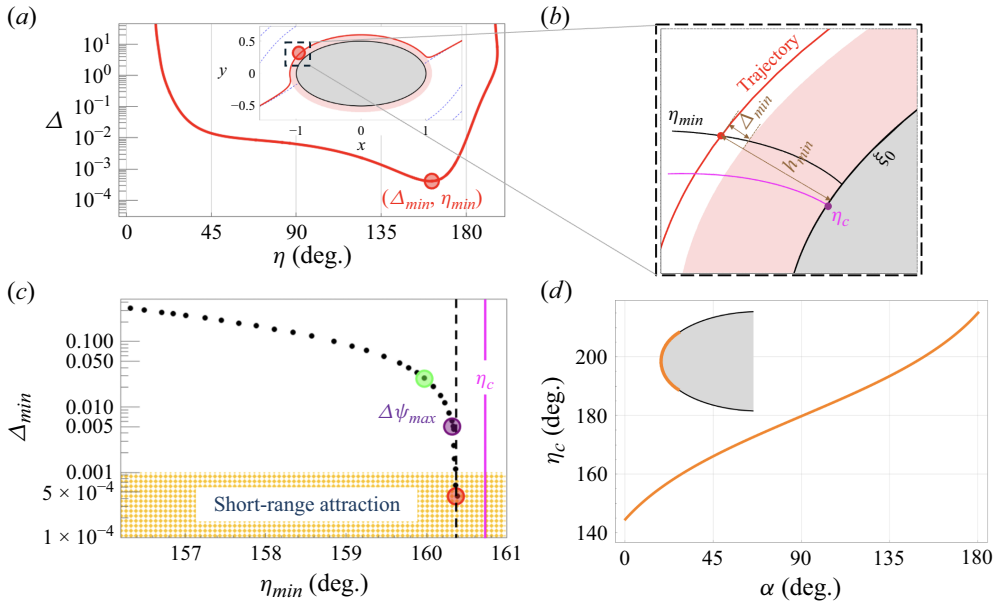


Figure 6. (*a*) Gap size Δ as a function of η along a 'dive' trajectory creeping around the obstacle (inset). (*b*) Close-up sketch near η_c demonstrating that the particle centre angular coordinate at closest approach η_{min} cannot coincide with η_c if $a_p > 0$. (*c*) Closest approach coordinates $(\Delta_{min}, \eta_{min})$ for different trajectories in the $\psi_i \to 0$ limit. Dashed line represents $\eta_{min}(\Delta_{min} = 0)$. While Δ_{min} varies by orders of magnitude, η_{min} stays close to the value η_c where flow curvature κ vanishes. Here $\Delta_{min} = O(10^{-3})$ represents a particle-to-surface wall gap of a few nanometres for a typical microparticle. Short-range intermolecular forces activate in this range and restrict particle movement. (*d*) Variation of η_c with α for $\beta = 1/2$, showing that particle sticking is always most likely near the major-axis tip of the ellipse.

(Nuritdinov *et al.* 2025; Sande *et al.* 2020; Uttam *et al.* 2023). Particles used for size-based sorting, selecting and trapping applications are often a few micrometres in size, so that a typical $\Delta_{min} = O(10^{-3})$ corresponds to a gap of a few nanometres, easily close enough for short-range attractions to be important.

Figure 6(*a*) plots $\Delta(\eta)$ along a dive trajectory, showing a well-defined closest approach point $(\Delta_{min}, \eta_{min})$. Changing ψ_i, figure 6(*c*) shows that Δ_{min} is very sensitive to initial conditions, but η_{min} is not. In fact, it follows from the wall-expansion approximation (2.10) that the closest approach is always determined by the point on the wall where $\kappa(\eta_c) = 0$, a function of background flow only. However, for finite particle size the angular position η_{min} of the particle where the dynamics is governed by η_c is slightly different, as illustrated in figure 6(*b*). It is easy to show that

$$\eta_c - \eta_{min} \sim a_p^2 \tag{4.16}$$

to leading order, so that even as $\psi_i \to 0$, a finite difference between η_{min} and η_c remains. For $a_p \ll 1$, practically relevant trajectories nevertheless have a very well-defined point of closest approach, to within a few degrees of η_c (figure 6*c*), and thus a well-defined location where sticking is most likely follows directly from the background flow wall curvature κ. The angular position η_c changes with the flow angle of attack α but not very widely. Figure 6(*d*) demonstrates that this point is located near the major-axis pole of the elliptic cylinder for all α.

In the case of internal Stokes flow confined by flat walls (Liu *et al.* 2025), the approach to minimum gap distance is well described by a single exponential, as predicted by theory

https://doi.org/10.1017/jfm.2026.11358 Published online by Cambridge University Press

(Brady & Bossis 1988; Claeys & Brady 1989, 1993). In the present case, the strong variation in $\kappa(\eta)$ with obstacle topography precludes such a simple behaviour. The direct comparison between our full (variable expansion) formalism and a pure wall expansion calculation in the inset of figure 3(*c*) confirms, however, that the decrease of Δ over orders of magnitude in proximity to η_c is governed by κ. The rapid approach in the presence of a variety of short-range forces will reliably lead to sticking at this predefined location. Pradel *et al.* (2024) in their latest research on particle accumulation in transport flow through porous media (similar to the asymmetric set-up of obstacles in a DLD device) emphasise the role of hydrodynamics to arrest a microparticle on the surface of a pore but did not establish any concrete mechanism on defining a specific location of single-particle capture. In this context, our mechanism offers valuable strategies for microfluidic filtration and particle capture in transport flow through porous media (Spielman 1977; Pradel *et al.* 2024; Miele *et al.* 2025).

5. Conclusions

The goal of our study has been to isolate the purely hydrodynamic displacement effect on a single force-free spherical particle encountering a cylindrical obstacle interface in zero-inertia transport flow. We show that one such encounter can indeed have a net displacement effect on particles when the geometry of the flow and obstacle breaks fore–aft symmetry. An exemplary case is an elliptic obstacle placed in a uniform flow with non-trivial angle of attack. Somewhat non-intuitively, there is a particular initial condition for given parameters for which the net displacement is maximal. For the practical case of particles much smaller than the obstacle ($a_p \ll 1$), this initial condition is very close to the separating streamline associated with the obstacle, and the maximum displacement (in terms of changes of streamfunction) is proportional to a_p^3 for eccentric obstacles. The effect is thus small, but also strongly dependent on particle size. A quantitative comparison with the effects of short-range roughness modelling shows comparable influence of obstacle symmetry breaking on the ability to separate microparticles by size. Thus, obstacle shape should be taken into account in set-ups pursuing such goals.

We find that the hydrodynamic displacement effects can be maximised by choosing a flow angle $\alpha = \pi/4$ and by decreasing the aspect ratio β of the ellipse, though corrections from obstacle surface curvature must be taken into account for very eccentric ellipses. These results do not contradict time reversibility: if time is reversed, all hydrodynamic forces also change sign together with the background flow, and particle paths are traced backwards.

While the present work puts the elementary hydrodynamic effects behind DLD on a firm footing, the practical DLD set-ups consist of many circular cylinders (pillars) arranged in an array under an inclination angle to the flow direction. One could approximate the effects on the flow of groups (e.g. two) of these circular cylinders by those of an effective elliptic cylinder, as the geometric motivation for symmetry breaking remains the same. We remark here that an analogous treatment of deflection from two circular cylinders should be possible, as flow solutions and trajectory geometry can be described in bipolar coordinates similar to the present-case elliptic coordinate system. Separating streamlines connecting two obstacles then become crucial boundaries that particles of different sizes do or do not cross, leading to DLD-like separation of particle paths by row-shifting, which has not been a subject of the present study.

The two-dimensional flow geometry in the present work was chosen both for simplicity and for its fundamental importance in a large class of microfluidic set-ups. Many other applications of force-free, inertialess particle manipulation use three-dimensional

https://doi.org/10.1017/jfm.2026.11358 Published online by Cambridge University Press

geometries, particularly in porous media filtration (Davis *et al.* 2006; Bordoloi *et al.* 2022; Miele *et al.* 2025). We remark that the modelling of boundary interactions employed here would be unchanged in this three-dimensional case as long as the particle sizes remain much smaller than both radii of curvature of the three-dimensional obstacle geometry. In order to quantitatively model a particular three-dimensional flow situation, though, it will be advantageous to connect the fundamental hydrodyamic interaction formalism developed here with a numerical Stokes flow simulation, which could deal with arbitrary geometries and also address challenges like noise and fluctuations.

In a microfluidic application with many particles, the present single-particle formalism is implicitly applicable to dilute concentrations. An important extension of this approach would be to incorporate particle–particle interactions, allowing for the assessment of non-inertial effects in particle-laden flows, which are crucial for many practical applications (Guha 2008). Another valuable generalisation of the current approach is to treat non-spherical particles, whose additional degrees of freedom allow for a wider range of qualitative trajectory behaviours (Yerasi, Govindarajan & Vincenzi 2022; Li *et al.* 2024; Liu 2025). In all cases, taking symmetry-breaking hydrodynamic interactions with boundaries into account will add a previously overlooked component to particle manipulation in any viscous flow situation.

Acknowledgements. The authors acknowledge valuable and inspiring conversations with J. Brady, B. Delmotte, C. Duprat, A. Lindner, B. Rallabandi and H. Stone.

Declaration of interests. The authors report no conflict of interest.

Appendix A. Wall-parallel correction factor $f(\Delta)$

As developed in Liu *et al.* (2025) by systematic asymptotic matching, the wall-parallel velocity correction factor $f(\Delta)$ takes the following form:

$$f(\Delta) = 1 - \frac{(1+\Delta)^4}{0.66 + 3.15\Delta + 5.06\Delta^2 + 3.73\Delta^3 + \Delta^4 - 0.27(1+\Delta)^4 \log\left(\frac{\Delta}{1+\Delta}\right)}. \quad \text{(A1)}$$

Figure 7(*a*) illustrates the agreement with the asymptote at $\Delta \gg 1$ (Goldman *et al.* 1967*a*) as well as the logarithmic approach to the lubrication-theory limit $f \to 1$ at $\Delta \to 0$ (Williams *et al.* 1992; Williams 1994). Equation (A1) is derived for a linear wall-parallel background velocity profile, which is asymptotically accurate for small Δ, the case of primary interest in this study.

Appendix B. Effect of the bulk Faxén correction

We have quantified the displacement along particle trajectories by streamfunction changes $\Delta\psi$ with respect to the reference flow ψ from (3.3) in order to explicitly quantify the wall effects only. Even without wall effects, the presence of the Faxén term (the effects of bulk flow curvature) can lead to changes along the particle trajectory between the initial and final background streamfunction values, $\Delta\psi_B = \Delta\psi_{B,i} - \Delta\psi_{B,f}$. Figure 7(*b*) shows that this Faxén contribution has a noticeable effect only for initial conditions that keep the particle far from the obstacle $\Delta \gtrsim 1$ throughout; yet in these cases, the displacement remains extremely small. For initial conditions of smaller ψ_i, which yield the important displacement effects discussed in the present work, the Faxén effect is at least one order of magnitude smaller than the wall effects.

https://doi.org/10.1017/jfm.2026.11358 Published online by Cambridge University Press

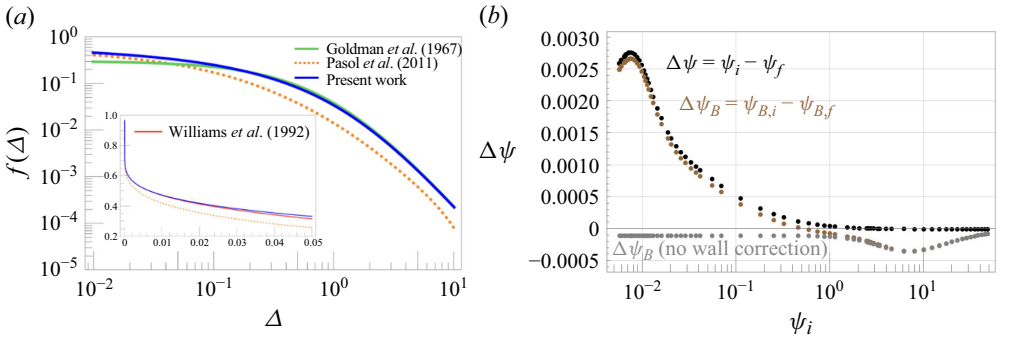


Figure 7. (*a*) Wall-parallel velocity correction factor $f(\Delta)$ as a function of non-dimensional gap Δ showing good agreement with Goldman *et al.* (1967*b*) in the far-field limit ($\Delta \gg 1$) and with Williams *et al.* (1992) (inset) near the wall ($\Delta \ll 1$), including the regime of lubrication theory. (*b*) Comparison of displacement effects (difference between final and initial streamfunction values along a trajectory) with the Faxén contribution subtracted out ($\Delta\psi$) or taken into account ($\Delta\psi_B$). Faxén effects are only noticeable for trajectories travelling at larger distances from the obstacle (having larger $\psi_i \gtrsim 1$), where displacements are very small. For smaller initial conditions ψ_i the displacements caused by the Faxén term alone (with no wall correction, grey) are insignificant compared with those caused by the wall effect. Here $(a_p, \alpha, \beta) = (0.1, 30°, 0.5)$.

Appendix C. Robustness of results against choice of modelling parameters

As mentioned in § 2.3 of the main text, the general approach to determining the wall-normal correction of the particle velocity at moderate to large Δ involves expanding the background velocity field around the particle centre position, cf. (2.8), while when the particle gets very close to touching the obstacle ($\Delta \to 0$) the description asymptotes to (2.10), where the velocity is expanded around a point at the obstacle wall. In order to smoothly transition from one description to the other, we introduce the variable expansion formalism (2.12), moving the expansion point continuously with the value of Δ, an approach already utilised in our recent study on particle dynamics in internal Stokes flows (Liu *et al.* 2025). We tested the robustness of this approach in the present case against changing the functional form of the expansion point dependence (2.13) to various nonlinear forms and found that variations are small as long as the overall smoothness of the transition is preserved. In figure 8(*a*), we show small quantitative differences upon changing the transition parameter $\Delta_E = \mathcal{O}(1)$ in (2.13), demonstrating that the displacement effect as a whole, and its maximum magnitude, are insensitive to such modelling changes. Our quantitative choice of Δ_E is motivated by evaluating the smoothness of the dependence of $W_\perp$ on Δ. This quantity is informed by flow gradients, which are locally stronger in the present case of external Stokes flow than in our previous work (in Liu *et al.* (2025) we used $\Delta_E = 1$), so that a slightly longer transition region of $\Delta_E = 3$ works best here.

As part of establishing the analytical model of $\Delta\psi$ from (4.5), we need to specify a gap value Δ^* to compute ψ_i^* and ψ_f^* from (4.6) and (4.7), respectively, as described in section § 4.2.2. We see from figure 8(*b*) that the choice of Δ^* in evaluating ψ_i^* and ψ_f^* only weakly affects the ultimate displacement $\Delta\psi = \psi_i^* - \psi_f^*$, as long as $\Delta^* \ll 1$, as the wall-expansion modelling formalism needs $\Delta \ll 1$ throughout on trajectories. In particular, the existence and position of a maximum in $\Delta\psi$ are robust against that choice. This motivated the simplified analytical treatment in § 4.2.3, where most quantities are evaluated at a distance of a_p from the obstacle, i.e. at $\Delta = 0$.

https://doi.org/10.1017/jfm.2026.11358 Published online by Cambridge University Press

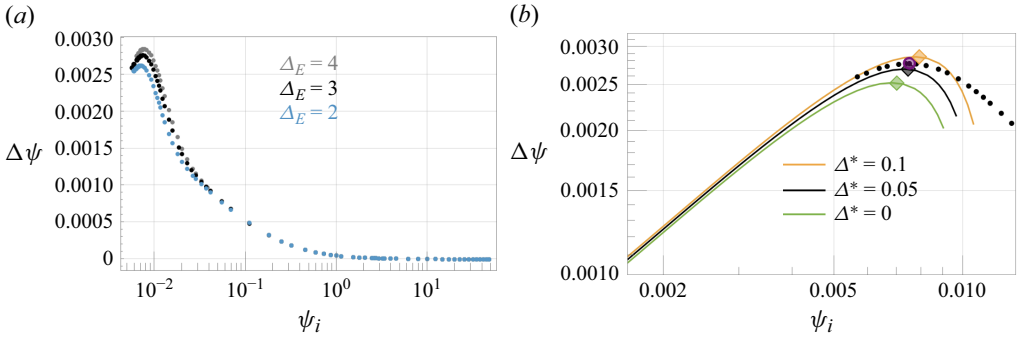


Figure 8. (*a*) Changing the value of the modelling parameter Δ_E in the variable expansion approach by $\mathcal{O}(1)$ factors only weakly affects the outcome of particle displacement. (*b*) Results for $\Delta\psi(\psi_i)$ computed from (4.5)–(4.7) with different choice of Δ^* according to the methodology discussed in § 4.2.2. Black dots are the results obtained from direct numerical analysis of trajectories (cf. § 4.2.1). Coloured symbols identify the positions of $\Delta\psi_{max}$. All results are for $(a_p, \alpha, \beta) = (0.1, 30°, 0.5)$.

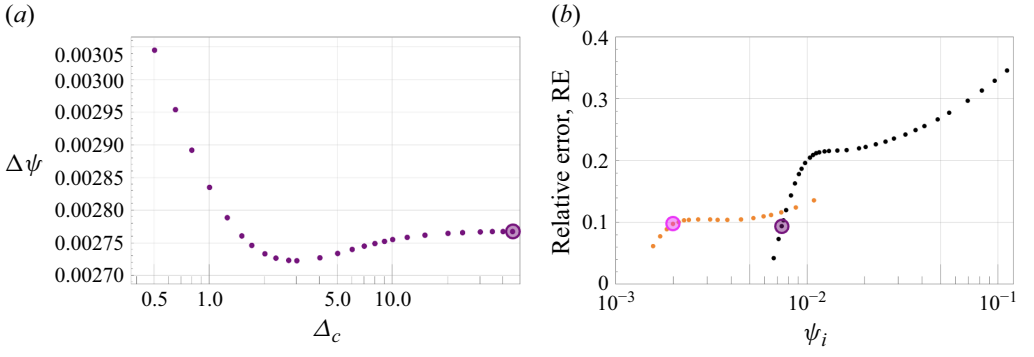


Figure 9. (*a*) Computation of $\Delta\psi$ for ψ_i corresponding to the 'purple' trajectory ($\Delta\psi_{max}$) in figure 4 with wall effect $W_\perp$ turned on for $\Delta < \Delta_c$; for results in the main text $W_\perp$ was turned on everywhere (purple circle on the right). The wall effects accumulated at $\Delta \gtrsim 1$ have negligible effect on the displacement, as choosing $\Delta_c \gtrsim 1$ does not affect the final outcome appreciably while a very late activation of $W_\perp$ misses some important effects. (*b*) Therefore, we recomputed $\Delta\psi$ for trajectories with $\Delta_{min} \lesssim 1$ taking wall curvature into account. Plotted is the relative error $\mathrm{RE} = (\Delta\psi_{curved\ wall} - \Delta\psi_{flat\ wall})/\Delta\psi_{curved\ wall}$ for two particle sizes, $a_p = 0.1$ in black and $a_p = 0.05$ in orange (magenta data correspond to $\Delta\psi_{max}$ for $a_p = 0.05$). Ignoring wall curvature when the wall effect is important ($\Delta_{min} \leqslant \Delta_c$) underestimates the deflection, but RE remains small ($< 10\,\%$) in computing the maximum deflection. The control parameters are $(\alpha, \beta) = (30°, 0.5)$.

Appendix D. Effect of wall curvature

The results presented in the main text are obtained from wall corrections assuming a flat wall (Rallabandi *et al.* 2017), which is self-consistent in the limit of small gaps, $\Delta < 1$. While it is intuitive that the majority of the wall interaction effects happen under this condition, one has to verify whether interactions at larger Δ accumulate to appreciable deflections and, if so, whether obstacle curvature must then be taken into account.

To address the first point, we present in figure 9(*a*) computations of $\Delta\psi$ along the 'purple'-type trajectory in figure 4 (exhibiting maximum displacement) where we only activate the wall effects for $\Delta < \Delta_c$, setting $W_\perp$ to zero for larger distances. The data presented in the main text are for $\Delta_c \sim 50$ (wall effects are activated everywhere, larger purple circle). The figure shows that wall effects are negligible for $\Delta_c \gtrsim 1$, confirming that (i) the vast majority of wall effect displacement happens at small Δ and (ii) the modelling

https://doi.org/10.1017/jfm.2026.11358 Published online by Cambridge University Press

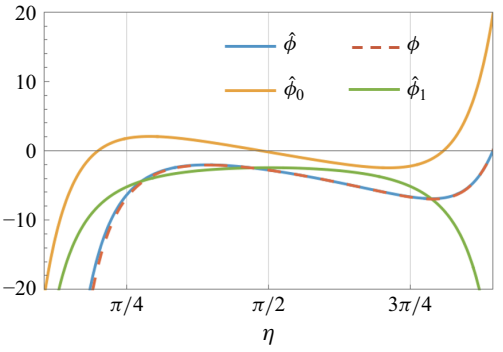


Figure 10. The analytically integrable function $\hat{\phi}$ as introduced in section § 4.2.3 is in excellent agreement with the ϕ function (4.4) developed in section § 4.2.2. We expand $\hat{\phi}$ in $\sin 2\alpha$ as $\hat{\phi} = \hat{\phi}_0 + \hat{\phi}_1 \sin 2\alpha + O(\sin^2 2\alpha)$ where the leading-order term $\hat{\phi}_0$ is antisymmetric but the first-order term $\hat{\phi}_1$ is symmetric around $\eta = \pi/2$. Here $(a_p, \alpha, \beta) \equiv (0.1, 30^\circ, 0.5)$.

of a distant elliptical obstacle at large distance as a flat wall does not introduce significant errors.

For the parts of the trajectory where $\Delta \leqslant \Delta_c$, is it important to model the finite curvature of the obstacle wall? We recomputed $\Delta\psi$ for the trajectories with $\Delta_{min} \leqslant 1$ using the curved-wall formalism developed for spherical obstacles in Rallabandi *et al.* (2017) by evaluating the radius of curvature R of the wall point closest to the particle by

$$R = \frac{1}{\beta}\left(\beta^2 \cos^2\eta + \sin^2\eta\right)^{3/2}. \tag{D1}$$

Figure 9(*b*) shows that the relative error in $\Delta\psi$ using the flat-wall formalism sharply drops for particles passing the obstacle at very close distance (in particular for trajectories near maximum deflection), while it becomes small throughout for smaller particles. Note that this computation likely overestimates the influence of curvature, as Rallabandi *et al.* (2017) describe the effect of a nearby spherical obstacle (two radii of curvature); qualitatively, our computation indicates that the displacements are slightly enhanced by curvature. However, because the curvature formalism is computationally expensive and does not introduce large errors, we use the flat-wall formalism for all computations presented in the main text.

Appendix E. Scaling of $\Delta\psi_{max}$ with parameters

The central quantity on which analytical computation of displacement hinges is the function $\phi(\eta)$ from (4.4) depicted in figure 10. We know that ϕ must be symmetric with respect to $\eta = \pi/2$ when $\alpha = 0$, and proceed to expand it for small α. Consistent to leading order, we choose $\sin 2\alpha$ as our expansion parameter, which conforms with the expected behaviour at larger α. Expanding as far as $\phi = \phi_0 + \phi_1 \sin 2\alpha$, (4.5) reads

$$\int_{\eta_f}^{\eta_i} (\phi_0 + \phi_1 \sin 2\alpha)\mathrm{d}\eta = 0. \tag{E1}$$

Making use of the simplified background streamfunction (4.8) and consistent evaluation of the terms in (4.4) at a_p distance to the obstacle ($\Delta \to 0$), we obtain analytically integrable versions of the two leading-order functions in (E1), namely

https://doi.org/10.1017/jfm.2026.11358 Published online by Cambridge University Press

$$\hat{\phi}_0 = \frac{(1-\beta^2)\left(3\beta^2 - 1 + \left(1-\beta^2\right)\cos 2\eta\right)}{\left(1-\left(1-\beta^2\right)\cos 2\eta + \beta^2\right)^{5/2}\tan\eta} \times \left(\cos 2\eta - \cosh\left(\frac{2\sqrt{2}a_p}{\sqrt{1-\left(1-\beta^2\right)\cos 2\eta + \beta^2}} + 2\tanh^{-1}\beta\right)\right) \tag{E2}$$

and

$$\hat{\phi}_1 = \frac{\beta(1-\beta^2)}{(1-(1-\beta^2)\cos 2\eta + \beta^2)(1-\cos 2\eta)} \times \left(\cos 2\eta - \cosh\left(\frac{2\sqrt{2}a_p}{\sqrt{1-\left(1-\beta^2\right)\cos 2\eta + \beta^2}} + 2\tanh^{-1}\beta\right)\right). \tag{E3}$$

As can be seen in figure 10, $\hat{\phi}_0$ is odd and $\hat{\phi}_1$ is even with respect to $\eta = \pi/2$ (and the sum of both terms is an excellent approximation of ϕ). However, integration over $\hat{\phi}_0$ from $\eta_i = \pi + \eta^{sep} - \Delta\eta_i$ to $\eta_f = \eta^{sep} + \Delta\eta_f$ does not respect these symmetries for two reasons: $\eta^{sep} \neq 0$ and $\delta = \Delta\eta_i - \Delta\eta_f \neq 0$. Both quantities do vanish as $\alpha \to 0$; from its definition we have $\eta^{sep} = (\beta/2)\sin 2\alpha$ to leading order and we write $\delta = \delta_1 \sin 2\alpha$ with δ_1 to be determined. Applying these definitions in (E1), all non-zero terms are proportional to $\sin 2\alpha$ and we obtain an explicit equation for δ_1:

$$\delta_1 = \frac{\int_{\eta=\Delta\eta_f}^{\eta=\pi-\Delta\eta_f} \hat{\phi}_1 \,\mathrm{d}\eta}{\hat{\phi}_0(\eta = \pi - \Delta\eta_f)} + \beta. \tag{E4}$$

Furthermore, we expand (E4) in small a_p and small $\Delta\eta_f$ to obtain

$$\delta_1 = 2\left[a_p \frac{(2-\beta^2)E\left(1-\frac{1}{\beta^2}\right) - K\left(1-\frac{1}{\beta^2}\right)}{\beta}\Delta\eta_f \right. \tag{E5}$$

$$\left. - \frac{\left(1-\beta^2\right)\left(\beta^2 + 3a_p\right)}{\beta^3}\Delta\eta_f^2 + O\left(\Delta\eta_f^3\right)\right] + O\left(a_p^2\right) \tag{E5}$$

with the complete elliptic integrals of first (K) and second (E) kind.

Equation (E5) computes δ, and thus η_i, from a given $\Delta\eta_f$, and thus η_f. To isolate the values for maximum particle deflection, we start with the definition of the extremum:

$$\frac{\partial\Delta\psi}{\partial\psi_i} = 0 \tag{E6}$$

and using the chain rule and the simplified streamfunction $\hat{\psi}_B$ from (4.8) to obtain

$$\frac{\partial\Delta\psi}{\partial\hat{\psi}_B} = \frac{\partial\Delta\psi}{\partial\hat{I}}\frac{\partial_\eta\hat{I}}{\partial_\eta\hat{\psi}_B}. \tag{E7}$$

One can find that both $\partial_\eta\hat{I} = \hat{\phi}$ and $\partial_\eta\hat{\psi}_B$ are non-zero over the range of η of interest for evaluating the maximum, so that we can instead use (4.10) as the maximum condition.

We here define $\zeta(\eta) \equiv \partial_\eta\hat{\psi}_B/\hat{\phi}$ (see § 4.2.3) and rewrite (4.11) as

$$\zeta(\eta_i = \pi + \eta^{sep} - \Delta\eta_f - \delta) = \zeta(\eta_f = \eta^{sep} + \Delta\eta_f). \tag{E8}$$

https://doi.org/10.1017/jfm.2026.11358 Published online by Cambridge University Press

Employing the same expansion in small δ as above, we find

$$\delta = \delta_1 \sin 2\alpha = \frac{\zeta(\eta = \pi + \eta^{sep} - \Delta\eta_f) - \zeta(\eta = \eta^{sep} + \Delta\eta_f)}{\partial_\eta \zeta|_{\eta=\pi+\eta^{sep}-\Delta\eta_f}}, \tag{E9}$$

and expansion of the right-hand side in small η^{sep} again yields terms proportional to $\sin 2\alpha$. Expanding in small a_p and $\Delta\eta$ results in another leading-order expression for δ_1:

$$\delta_1 = \left[6a_p \frac{1-\beta^2}{\beta^3}\Delta\eta_f^2 + O\left(\Delta\eta_f^3\right)\right] + O\left(a_p^2\right). \tag{E10}$$

Solving (E5) and (E10) simultaneously for δ_1 and $\Delta\eta_f$, we obtain the expressions (4.12) and (4.13). These equations can be evaluated in the limit of $\beta \ll 1$ to yield

$$\Delta\eta_f = \frac{\beta}{3}, \tag{E11}$$

$$\delta_1 = \frac{2}{3}\frac{a_p}{\beta}, \tag{E12}$$

which after insertion in (4.14) obtains the analytical limit of $\Delta\psi_{max}$ for small β as given in (4.15). Note that only the δ_1 terms in (4.14) contribute in this limit.

References

Agarwal, S. 2021 Rectified inertial forces on spherical particles in oscillatory fluid flows near interfaces. PhD thesis, University of Illinois Urbana–Champaign.

Agarwal, S., Chan, F.K., Rallabandi, B., Gazzola, M. & Hilgenfeldt, S. 2021 An unrecognized inertial force induced by flow curvature in microfluidics. *Proc. Natl Acad. Sci.* **118** (29), e2103822118.

Agarwal, S., Rallabandi, B. & Hilgenfeldt, S. 2018 Inertial forces for particle manipulation near oscillating interfaces. *Phys. Rev. Fluids* **3** (10), 104201.

Agarwal, S., Upadhyay, G., Bhosale, Y., Gazzola, M. & Hilgenfeldt, S. 2024 Density-contrast induced inertial forces on particles in oscillatory flows. *J. Fluid Mech.* **985**, A33.

Aghilinejad, A., Aghaamoo, M. & Chen, X. 2019 On the transport of particles/cells in high-throughput deterministic lateral displacement devices: implications for circulating tumor cell separation. *Biomicrofluidics* **13** (3), 034112.

Ashkin, A., Dziedzic, J.M., Bjorkholm, J.E. & Chu, S. 1986 Observation of a single-beam gradient force optical trap for dielectric particles. *Opt. Lett.* **11** (5), 288–290.

Ateya, D.A., Erickson, J.S., Howell, P.B., Hilliard, L.R., Golden, J.P. & Ligler, F.S. 2008 The good, the bad, and the tiny: a review of microflow cytometry. *Anal. Bioanal. Chem.* **391**, 1485–1498.

Balvin, M., Sohn, E., Iracki, T., Drazer, G. & Frechette, J. 2009 Directional locking and the role of irreversible interactions in deterministic hydrodynamics separations in microfluidic devices. *Phys. Rev. Lett.* **103** (7), 078301.

Batchelor, G.K. 2000 *An Introduction to Fluid Dynamics*. Cambridge University Press.

Berry, A.J. & Swain, L.M. 1923 On the steady motion of a cylinder through infinite viscous fluid. *Proc. R. Soc. Lond. Series A Contain. Papers Math. Phys. Char.* **102** (719), 766–778.

Blanc, F., Peters, F. & Lemaire, E. 2011 Experimental signature of the pair trajectories of rough spheres in the shear-induced microstructure in noncolloidal suspensions. *Phys. Rev. Lett.* **107** (20), 208302.

Bordoloi, A.D., Scheidweiler, D., Dentz, M., Bouabdellaoui, M., Abbarchi, M. & De Anna, P. 2022 Structure induced laminar vortices control anomalous dispersion in porous media. *Nat. Commun.* **13** (1), 3820.

Bowman, T.J., Drazer, G. & Frechette, J. 2013 Inertia and scaling in deterministic lateral displacement. *Biomicrofluidics* **7** (6), 064111.

Brady, J.F. & Bossis, G. 1988 Stokesian dynamics. *Annu. Rev. Fluid Mech.* **20** (1), 111–157.

Brenner, H. 1961 The slow motion of a sphere through a viscous fluid towards a plane surface. *Chem. Engng Sci.* **16** (3-4), 242–251.

Callow, J.A. & Callow, M.E. 2011 Trends in the development of environmentally friendly fouling-resistant marine coatings. *Nat. Commun.* **2** (1), 244.

Cerbelli, S. 2012 Separation of polydisperse particle mixtures by deterministic lateral displacement. The impact of particle diffusivity on separation efficiency. *Asia-Pac. J. Chem. Engng* **7**, S356–S371.

https://doi.org/10.1017/jfm.2026.11358 Published online by Cambridge University Press

CHAMOLLY, A., LAUGA, E. & TOTTORI, S. 2020 Irreversible hydrodynamic trapping by surface rollers. *Soft Matter* **16** (10), 2611–2620.

CHIOU, P.Y., OHTA, A.T. & WU, M.C. 2005 Massively parallel manipulation of single cells and microparticles using optical images. *Nature* **436** (7049), 370–372.

CLAEYS, I.L. & BRADY, J.F. 1989 Lubrication singularities of the grand resistance tensor for two arbitrary particles. *PhysicoChem Hydrodyn.* **11** (3), 261–293.

CLAEYS, I.L. & BRADY, J.F. 1993 Suspensions of prolate spheroids in Stokes flow. Part 1. Dynamics of a finite number of particles in an unbounded fluid. *J. Fluid Mech.* **251**, 411–442.

CRICK, F.H.C. & HUGHES, A.F.W. 1950 The physical properties of cytoplasm: a study by means of the magnetic particle method. Part I. Experimental. *Exper. Cell Res.* **1** (1), 37–80.

DA CUNHA, F.R. & HINCH, E.J. 1996 Shear-induced dispersion in a dilute suspension of rough spheres. *J. Fluid Mech.* **309**, 211–223.

DANCE, S.L., CLIMENT, E. & MAXEY, M.R. 2004 Collision barrier effects on the bulk flow in a random suspension. *Phys. Fluids* **16** (3), 828–831.

DAVIS, J.A., INGLIS, D.W., MORTON, K.J., LAWRENCE, D.A., HUANG, L.R., CHOU, S.Y., STURM, J.C. & AUSTIN, R.H. 2006 Deterministic hydrodynamics: taking blood apart. *Proc. Natl Acad. Sci.* **103** (40), 14779–14784.

DI CARLO, D. 2009 Inertial microfluidics. *Lab on a Chip* **9** (21), 3038–3046.

DI CARLO, D., IRIMIA, D., TOMPKINS, R.G. & TONER, M. 2007 Continuous inertial focusing, ordering, and separation of particles in microchannels. *Proc. Natl Acad. Sci.* **104** (48), 18892–18897.

DITTRICH, P.S. & MANZ, A. 2006 Lab-on-a-chip: microfluidics in drug discovery. *Nat. Rev. Drug Discov.* **5** (3), 210–218.

EKIEL-JEŻEWSKA, M.L., FEUILLEBOIS, F., LECOQ, N., MASMOUDI, K., ANTHORE, R., BOSTEL, F. & WAJNRYB, E. 1999 Hydrodynamic interactions between two spheres at contact. *Phys. Rev. E* **59** (3), 3182.

EKIEL-JEŻEWSKA, M.L. & WAJNRYB, E. 2006 Accuracy of the multipole expansion applied to a sphere in a creeping flow parallel to a wall. *Quart. J. Mech. Appl. Math.* **59** (4), 563–585.

FRECHETTE, J. & DRAZER, G. 2009 Directional locking and deterministic separation in periodic arrays. *J. Fluid Mech.* **627**, 379–401.

GATIGNOL, R. 1983 The faxén formulae for a rigid particle in an unsteady non-uniform stokes flow. *J. Mec. Theor. Appl.* **2** (2), 143–160.

GOLDMAN, A.J., COX, R.G. & BRENNER, H. 1967*a* Slow viscous motion of a sphere parallel to a plane wall—II Couette flow. *Chem. Engng Sci.* **22** (4), 653–660.

GOLDMAN, A.J., COX, R.G. & BRENNER, H. 1967*b* Slow viscous motion of a sphere parallel to a plane wall—I Motion through a quiescent fluid. *Chem. Engng Sci.* **22** (4), 637–651.

GOSSE, C. & CROQUETTE, V. 2002 Magnetic tweezers: micromanipulation and force measurement at the molecular level. *Biophys. J.* **82** (6), 3314–3329.

GOSSETT, D.R., WEAVER, W.M., MACH, A.J., HUR, S.C., TSE, H.T.K., LEE, W., AMINI, H. & DI CARLO, D. 2010 Label-free cell separation and sorting in microfluidic systems. *Anal. Bioanal. Chem.* **397**, 3249–3267.

GRIER, D.G. 2003 A revolution in optical manipulation. *Nature* **424** (6950), 810–816.

GUHA, A. 2008 Transport and deposition of particles in turbulent and laminar flow. *Annu. Rev. Fluid Mech.* **40** (1), 311–341.

GUL, A., HRUZA, J. & YALCINKAYA, F. 2021 Fouling and chemical cleaning of microfiltration membranes: a mini-review. *Polymers* **13** (6), 846.

HAPPEL, J. & BRENNER, H. 1965 *Low Reynolds Number Hydrodynamics: With Special Applications to Particulate Media*. Prentice-Hall.

HOCHSTETTER, A., VERNEKAR, R., AUSTIN, R.H., BECKER, H., BEECH, J.P., FEDOSOV, D.A., GOMPPER, G., KIM, S.-C., SMITH, J.T. & STOLOVITZKY, G. 2020 Deterministic lateral displacement: challenges and perspectives. *ACS Nano* **14** (9), 10784–10795.

HUANG, L.R., COX, E.C., AUSTIN, R.H. & STURM, J.C. 2004 Continuous particle separation through deterministic lateral displacement. *Science* **304** (5673), 987–990.

HÜLAGÜ, D., TOBIAS, C., DAO, R., KOMAROV, P., RURACK, K. & HODOROABA, V.-D. 2024 Towards 3D determination of the surface roughness of core–shell microparticles as a routine quality control procedure by scanning electron microscopy. *Sci. Rep.* **14** (1), 17936.

INGLIS, D.W., DAVIS, J.A., AUSTIN, R.H. & STURM, J.C. 2006 Critical particle size for fractionation by deterministic lateral displacement. *Lab on a Chip* **6** (5), 655–658.

KABACAOĞLU, G. & BIROS, G. 2019 Sorting same-size red blood cells in deep deterministic lateral displacement devices. *J. Fluid Mech.* **859**, 433–475.

https://doi.org/10.1017/jfm.2026.11358 Published online by Cambridge University Press

KANG, L., CHUNG, B.G., LANGER, R. & KHADEMHOSSEINI, A. 2008 Microfluidics for drug discovery and development: from target selection to product lifecycle management. *Drug Discov. Today* **13** (1-2), 1–13.
KAPLUN, S. 1957 Low Reynolds number flow past a circular cylinder. *J. Math. Mech.* **6**, 595–603.
KIM, S. & KARRILA, S.J. 2013 *Microhydrodynamics: Principles and Selected Applications*. Butterworth-Heinemann.
KIRSCHNER, C.M. & BRENNAN, A.B. 2012 Bio-inspired antifouling strategies. *Ann. Rev. Mater. Res.* **42**, 211–229.
KRÜGER, T., HOLMES, D. & COVENEY, P.V.2014 Deformability-based red blood cell separation in deterministic lateral displacement devices – a simulation study. *Biomicrofluidics* **8** (5), 054114.
KULRATTANARAK, T., VAN DER SMAN, R.G.M., SCHROËN, C.G.P.H. & BOOM, R.M. 2011 Analysis of mixed motion in deterministic ratchets via experiment and particle simulation. *Microfluid. Nanofluid.* **10**, 843–853.
KUMAR, D., SHENOY, A., LI, S. & SCHROEDER, C.M. 2019 Orientation control and nonlinear trajectory tracking of colloidal particles using microfluidics. *Phys. Rev. Fluids* **4** (11), 114203.
KUMAR, R. & ISMAIL, A.F. 2015 Fouling control on microfiltration/ultrafiltration membranes: effects of morphology, hydrophilicity, and charge. *J. Appl. Polym. Sci.* **132** (21), 42042.
LEMAIRE, E., BLANC, F., CLAUDET, C., GALLIER, S., LOBRY, L. & PETERS, F. 2023 Rheology of non-brownian suspensions: a rough contact story. *Rheol. Acta* **62** (5), 253–268.
LENSHOF, A. & LAURELL, T. 2010 Continuous separation of cells and particles in microfluidic systems. *Chem. Soc. Rev.* **39** (3), 1203–1217.
LI, Z., BIELINSKI, C., LINDNER, A., DU ROURE, O. & DELMOTTE, B. 2024 Dynamics of rigid fibers interacting with triangular obstacles in microchannel flows. *Phys. Rev. Fluids* **9** (4), 044302.
LIN, A. & HAN, S.-P. 2002 On the distance between two ellipsoids. *SIAM J. Optimiz.* **13** (1), 298–308.
LIU, X. 2025 Particle manipulation by hydrodynamic effects in vortical stokes flow. PhD thesis, University of Illinois Urbana-Champaign.
LIU, X., DAS, P.K. & HILGENFELDT, S. 2025 Principles of hydrodynamic particle manipulation in internal Stokes flow. *J. Fluid Mech.* **1007**, A33.
LU, N., *et al.* 2023 Label-free microfluidic cell sorting and detection for rapid blood analysis. *Lab on a Chip* **23** (5), 1226–1257.
LU, X., LIU, C., HU, G. & XUAN, X. 2017 Particle manipulations in non-Newtonian microfluidics: a review. *J. Colloid Interface Sci.* **500**, 182–201.
LUTZ, B.R., CHEN, J. & SCHWARTZ, D.T. 2006 Hydrodynamic tweezers: 1. Noncontact trapping of single cells using steady streaming microeddies. *Anal. Chem.* **78** (15), 5429–5435.
MAXEY, M.R. & RILEY, J.J. 1983 Equation of motion for a small rigid sphere in a nonuniform flow. *Phys. Fluids* **26** (4), 883–889.
MAYS, D.C. & HUNT, J.R. 2005 Hydrodynamic aspects of particle clogging in porous media. *Environ. Sci. Technol.* **39** (2), 577–584.
METZGER, B. & BUTLER, J.E. 2010 Irreversibility and chaos: role of long-range hydrodynamic interactions in sheared suspensions. *Phys. Rev. E* **82** (5), 051406.
MIELE, F., BORDOLOI, A.D., DENTZ, M., TABUTEAU, H., MORALES, V.L. & DE ANNA, P. 2025 Flow induced intermittent transport shapes colloid filtration in complex media. arXiv:2505.02689.
NGUYEN, N.-T., SHAEGH, S.A.M., KASHANINEJAD, N. & PHAN, D.-T. 2013 Design, fabrication and characterization of drug delivery systems based on lab-on-a-chip technology. *Adv. Drug Deliver. Rev.* **65** (11–12), 1403–1419.
NILSSON, J., EVANDER, M., HAMMARSTRÖM, B. & LAURELL, T. 2009 Review of cell and particle trapping in microfluidic systems. *Anal. Chim. Acta* **649** (2), 141–157.
NIR, S. & RECHES, M. 2016 Bio-inspired antifouling approaches: the quest towards non-toxic and non-biocidal materials. *Curr. Opin. Biotech.* **39**, 48–55.
NURITDINOV, F., *et al.* 2025 Experimental system enables studies of *Mycobacterium tuberculosis* during aerogenic transmission. *mBio* **16** (10), e00958–e00925.
PAMME, N. 2007 Continuous flow separations in microfluidic devices. *Lab on a Chip* **7** (12), 1644–1659.
PARISET, E., PUDDA, C., BOIZOT, F., VERPLANCK, N., BERTHIER, J., THUAIRE, A. & AGACHE, V. 2017 Anticipating cutoff diameters in deterministic lateral displacement (DLD) microfluidic devices for an optimized particle separation. *Small* **13** (37), 1701901.
PASOL, L., MARTIN, M., EKIEL-JEŻEWSKA, M.L., WAJNRYB, E., BŁAWZDZIEWICZ, J. & FEUILLEBOIS, F. 2011 Motion of a sphere parallel to plane walls in a Poiseuille flow. Application to field-flow fractionation and hydrodynamic chromatography. *Chem. Engng Sci.* **66** (18), 4078–4089.

https://doi.org/10.1017/jfm.2026.11358 Published online by Cambridge University Press

PETIT, T., ZHANG, L., PEYER, K.E., KRATOCHVIL, B.E. & NELSON, B.J. 2012 Selective trapping and manipulation of microscale objects using mobile microvortices. *Nano Lett.* **12** (1), 156–160.

PHAM, P., METZGER, B. & BUTLER, J.E. 2015 Particle dispersion in sheared suspensions: crucial role of solid-solid contacts. *Phys. Fluids* **27** (5), 051701.

POZRIKIDIS, C. 1992 *Boundary Integral and Singularity Methods for Linearized Viscous Flow*. Cambridge University Press.

POZRIKIDIS, C. 2011 *Introduction to Theoretical and Computational Fluid Dynamics*. Oxford University Press.

PRADEL, A., DELOUCHE, N., GIGAULT, J. & TABUTEAU, H. 2024 Role of ripening in the deposition of fragments: the case of micro-and nanoplastics. *Environ. Sci. Technol.* **58** (20), 8878–8888.

PRATT, E.D., HUANG, C., HAWKINS, B.G., GLEGHORN, J.P. & KIRBY, B.J. 2011 Rare cell capture in microfluidic devices. *Chem. Engng Sci.* **66** (7), 1508–1522.

PROUDMAN, I. & PEARSON, J.R.A. 1957 Expansions at small Reynolds numbers for the flow past a sphere and a circular cylinder. *J. Fluid Mech.* **2** (3), 237–262.

PURI, I.K. & GANGULY, R. 2014 Particle transport in therapeutic magnetic fields. *Annu. Rev. Fluid Mech.* **46**, 407–440.

RAJENDRAN, D.S., DEVI, E.G., SUBIKSHAA, V.S., SETHI, P., PATIL, A., CHAKRABORTY, A., VENKATARAMAN, S. & KUMAR, V.V. 2025 Recent advances in various cleaning strategies to control membrane fouling: a comprehensive review. *Clean Technol. Environ. Policy* **27** (2), 649–664.

RALLABANDI, B. 2021 Inertial forces in the Maxey–Riley equation in nonuniform flows. *Phys. Rev. Fluids* **6** (1), L012302.

RALLABANDI, B., HILGENFELDT, S. & STONE, H.A. 2017 Hydrodynamic force on a sphere normal to an obstacle due to a non-uniform flow. *J. Fluid Mech.* **818**, 407–434.

RAYNOR, P.C. 2002 Flow field and drag for elliptical filter fibers. *Aerosol Sci. Technol.* **36** (12), 1118–1127.

SAJEESH, P. & SEN, A.K. 2014 Particle separation and sorting in microfluidic devices: a review. *Microfluid. Nanofluid.* **17**, 1–52.

SANDE, M.G., ÇAYKARA, T., SILVA, C.J. & RODRIGUES, L.R. 2020 New solutions to capture and enrich bacteria from complex samples. *Med. Microbiol. Immun.* **209** (3), 335–341.

SHENOY, A., RAO, C.V. & SCHROEDER, C.M. 2016 Stokes trap for multiplexed particle manipulation and assembly using fluidics. *Proc. Natl Acad. Sci.* **113** (15), 3976–3981.

SHINTANI, K., UMEMURA, A. & TAKANO, A. 1983 Low-reynolds-number flow past an elliptic cylinder. *J. Fluid Mech.* **136**, 277–289.

SMART, J.R. & LEIGHTON, D.T.Jr 1989 Measurement of the hydrodynamic surface roughness of noncolloidal spheres. *Phys. Fluids A* **1** (1), 52–60.

SPIELMAN, L.A. 1977 Particle capture from low-speed laminar flows. *Annu. Rev. Fluid Mech.* **9** (1), 297–319.

TANYERI, M., RANKA, M., SITTIPOLKUL, N. & SCHROEDER, C.M. 2011 A microfluidic-based hydrodynamic trap: design and implementation. *Lab on a Chip* **11** (10), 1786–1794.

THAMEEM, R., RALLABANDI, B. & HILGENFELDT, S. 2017 Fast inertial particle manipulation in oscillating flows. *Phys. Rev. Fluids* **2** (5), 052001.

UTTAM, I., SUDARSAN, S., RAY, R., CHINNAPPAN, R., YAQINUDDIN, A., AL-KATTAN, K. & MANI, N.K. 2023 A hypothetical approach to concentrate microorganisms from human urine samples using paper-based adsorbents for point-of-care molecular assays. *Life* **14** (1), 38.

VAN REENEN, A., DE JONG, A.M., DEN TOONDER, J.M.J., JAAP, M.J. & PRINS, M.W.J. 2014 Integrated lab-on-chip biosensing systems based on magnetic particle actuation–a comprehensive review. *Lab on a Chip* **14** (12), 1966–1986.

WANG, C., JALIKOP, S.V. & HILGENFELDT, S. 2011 Size-sensitive sorting of microparticles through control of flow geometry. *Appl. Phys. Lett.* **99** (3), 034101.

WANG, C., JALIKOP, S.V. & HILGENFELDT, S. 2012 Efficient manipulation of microparticles in bubble streaming flows. *Biomicrofluidics* **6** (1), 012801.

WANG, N., BUTLER, J.P. & INGBER, D.E. 1993 Mechanotransduction across the cell surface and through the cytoskeleton. *Science* **260** (5111), 1124–1127.

WIKLUND, M., GREEN, R. & OHLIN, M. 2012 Acoustofluidics 14: applications of acoustic streaming in microfluidic devices. *Lab on a Chip* **12** (14), 2438–2451.

WILLIAMS, P.S. 1994 Particle trajectories in field-flow fractionation and splitt fractionation channels. *Sep. Sci. Technol.* **29** (1), 11–45.

WILLIAMS, P.S., KOCH, T. & GIDDINGS, C.J. 1992 Characterization of near-wall hydrodynamic lift forces using sedimentation field-flow fractionation. *Chem. Engng Commun.* **111** (1), 121–147.

https://doi.org/10.1017/jfm.2026.11358 Published online by Cambridge University Press

XUAN, X. 2019 Recent advances in direct current electrokinetic manipulation of particles for microfluidic applications. *Electrophoresis* **40** (18-19), 2484–2513.

XUAN, X., ZHU, J. & CHURCH, C. 2010 Particle focusing in microfluidic devices. *Microfluid Nanofluid* **9**, 1–16.

YANG, S., ZHANG, H. & HSU, S.M. 2007 Correction of random surface roughness on colloidal probes in measuring adhesion. *Langmuir* **23** (3), 1195–1202.

YERASI, S.R., GOVINDARAJAN, R. & VINCENZI, D. 2022 Spirographic motion in a vortex. *Phys. Rev. Fluids* **7** (7), 074402.

https://doi.org/10.1017/jfm.2026.11358 Published online by Cambridge University Press